Reconfigurable Antennas for High Data Rate Multi-beam Communication Systems

Final Progress Report- Summary of Research

Principle Investigator: Prof. Jennifer T. Bernhard
Co-Investigator: Prof. Eric Michielssen
Reporting Period: March 1, 2001 – November 30, 2004
Address: University of Illinois at Urbana-Champaign
Department of Electrical and Computer Engineering
1406 W. Green Street, MC 702
Urbana, IL 61801

NASA Research Grant Number NAG3-2555

Program Monitor: Dr. Afroz Zaman
NASA Glenn Research Center
MS 54-8
Applied RF Technology Branch
21000 Brookpark Road
Cleveland, OH 44135-3191

Reconfigurable Antennas for High Data Rate Multi-beam Communication Systems

Final Progress Report- Summary of Research

Principle Investigator: Prof. Jennifer T. Bernhard
Co-Investigator: Prof. Eric Michielssen
Reporting Period: March 1, 2001 – November 30, 2004
Address: University of Illinois at Urbana-Champaign
Department of Electrical and Computer Engineering
1406 W. Green Street, MC 702
Urbana, IL 61801

NASA Research Grant Number NAG3-2555

Program Monitor: Dr. Afroz Zaman
NASA Glenn Research Center
MS 54-8
Applied RF Technology Branch
21000 Brookpark Road
Cleveland, OH 44135-3191

Project Overview

High-speed (2-100 Mb/sec) wireless data communication – whether land- or satellite-based – faces a major challenge: high error rates caused by interference and unpredictable environments. A planar antenna system that can be reconfigured to respond to changing conditions has the potential to dramatically improve data throughput and system reliability. Moreover, new planar antenna designs that reduce array size, weight, and cost can have a significant impact on terrestrial and satellite communication system performance.

This research developed new individually-reconfigurable planar antenna array elements that can be adjusted to provide multiple beams while providing increased scan angles and higher aperture efficiency than traditional diffraction-limited arrays. These new elements are microstrip spiral antennas with specialized tuning mechanisms that provide adjustable radiation patterns. We anticipate that these new elements can be used in both large and small arrays for inter-satellite communication as well as tracking of multiple mobile surface-based units.

Technical Summary

Our work has developed both theoretical descriptions as well as experimental prototypes of the antennas in both single element and array embodiments. The technical summary of the results of this work is divided into six sections:

A. Cavity model for analysis and design of pattern reconfigurable antennas
B. Performance of antenna in array configurations for broadside and endfire operation
C. Performance of antenna in array configurations for beam scanning operation
D. Simulation of antennas in infinite phased arrays
E. Demonstration of antenna with commercially-available RF MEMS switches
F. Design of antenna/RF MEMS switch combinations for direct simultaneous fabrication

A. Cavity Model of the Pattern Reconfigurable Antenna

A cavity model [1] of a radiation and frequency reconfigurable microstrip square spiral antenna [2] has been developed. This type of model provides physical insight into the operation of the antenna, which can serve as a foundation for the development of a generalized design methodology. In general, the versatility of the cavity model makes it very suitable for the analysis of numerous devices. It has proven to be a powerful analysis tool, and has demonstrated this outside the realm of traditional microstrip patch antennas [e.g., 6 and 7] with good success. Overall, this method provides straightforward results and an excellent physical interpretation of the radiating mechanisms associated with the antenna, along with a solid foundation for understanding the operation with respect to frequency. The model may then be used as the basis for a design methodology that can be used for new substrates, frequencies, and radiation requirements.

A.1 Reconfigurable Antenna Geometry and Behavior

The reconfigurable antenna geometry discussed in [2] is capable of switching between broadside and endfire radiation characteristics, maintained over a common impedance bandwidth centered around 6.85 GHz. The total linear dimension of the antenna is 81 mm (~2.5 λ_{eff}), and it is fabricated on Duroid 5880 substrate with $\varepsilon_r = 2.2$ and $h = 3.175$ mm (approximately 0.07λ at 6.85 GHz). The antenna geometry can be seen in Figure A.1, and all relevant dimensions of the

antenna are given in Table A.1. The total footprint of the antenna is approximately $0.5\lambda_0$ x $0.5\lambda_0$ at 6.9 GHz. To excite the antenna, a vertical SMA probe (diameter = 1.23 mm) is connected to the interior end of the spiral. The outer end of the spiral is shorted to ground with a copper via (diameter = 1.23 mm).

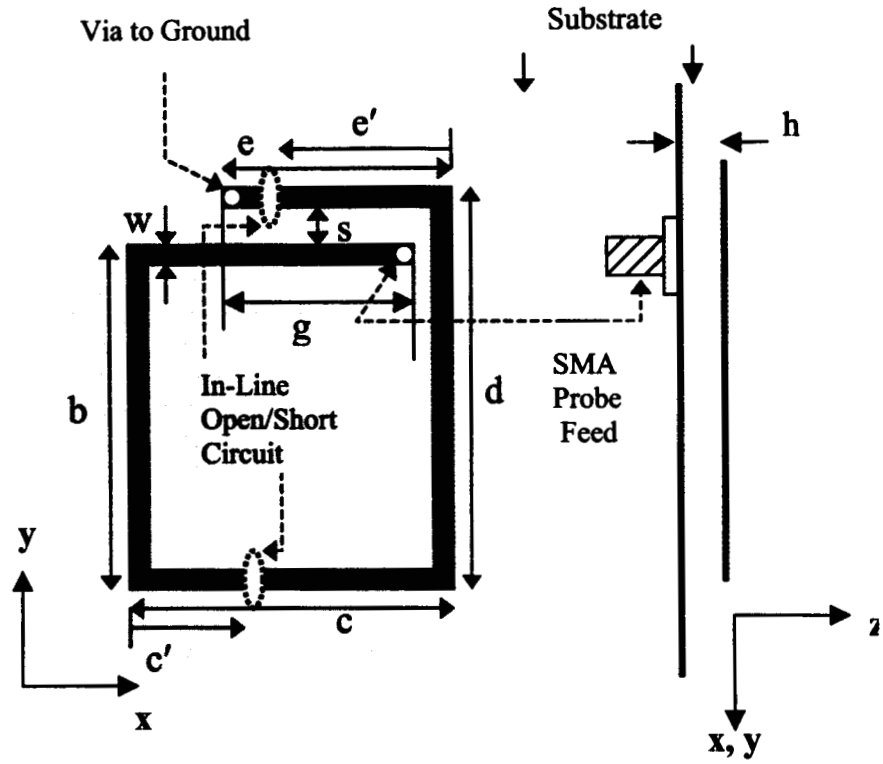

Figure A.1: Antenna geometry and orientation for reconfigured radiation configurations. In the endfire configuration, the switch at e' is open and the switch at c' is closed, forming the square spiral geometry. For the broadside configuration the switch at c' is open and the switch at e' is closed, separating the spiral into the probe fed section and shorted parasitic section.

Table A.1. Dimensions (mm) for the antenna geometry in Figure A.1.

a	b	c	c′	d	e	e′	g	w	s	h
16.0	18.0	18.0	7.0	22.25	12.0	8.5	12	1.0	1.25	3.175

A.2 Operation

To alter the standing electric field distribution on the structure and reconfigure the radiation patterns, two surface mountable switching elements of dimension 1.0 mm x 1.0 mm (currently hard-wired for proof of concept) are incorporated into the design. For impedance tuning purposes, the local position of these switching elements may be properly adjusted to achieve the desired impedance match. In the endfire configuration, the switch location at c' is closed and the switch location at e' is open. With this switch combination, the single turn square spiral geometry is created. In the broadside configuration, the switch location at c' is open and the switch location at e' is closed. In this switch configuration the antenna is composed of two

separate sections: the probe-fed section and the grounded parasitic section which is excited via coupling across the contiguous section of length f, separated by the distance s. The impedance, VSWR and elevation radiation patterns have been measured and are shown in Figures A.2 – A.5, respectively, with the results obtained from simulations of this structure in HFSS 9.1 included in Figures A.3 – A.5. The overall shared VSWR bandwidth (Figure 3) is shifted slightly down in frequency, which can be explained by a slight probe feed off-set during fabrication. For the pattern behavior (Figures A.4 and A.5), the simulated and measured radiation patterns are taken at the center of their respective shared bandwidths (~ 6.78 GHz and ~6.85 GHz).

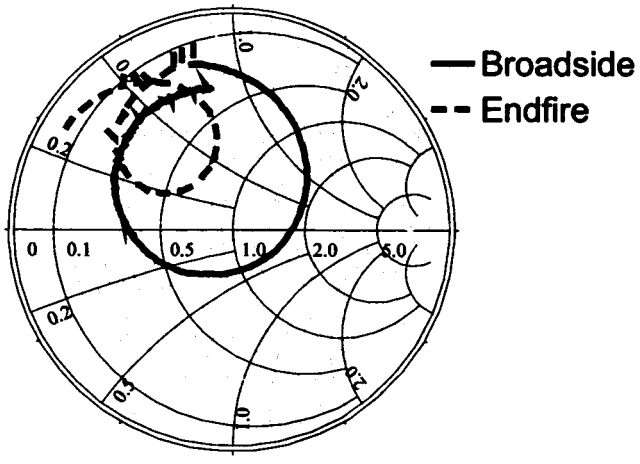

Figure A.2: Input impedance of broadside and endfire radiation configurations.

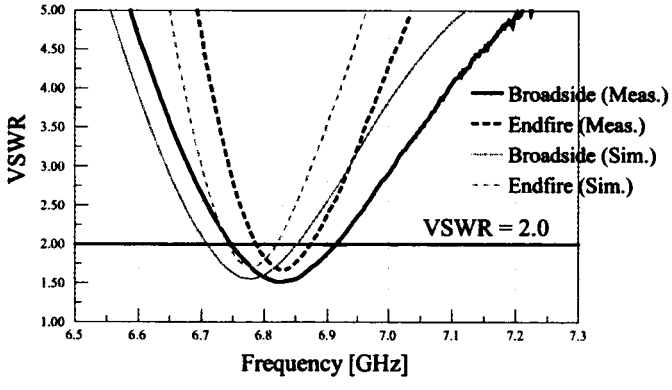

Figure A.3: Measured (black) and HFSS simulated (grey) VSWR of broadside (solid) and endfire (dashed) radiation configurations.

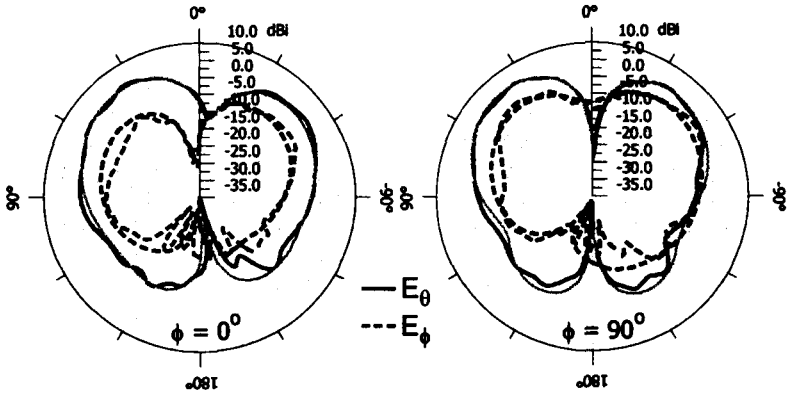

Figure A.4: Measured (black) and HFSS simulated (grey) radiation pattern of endfire configuration.

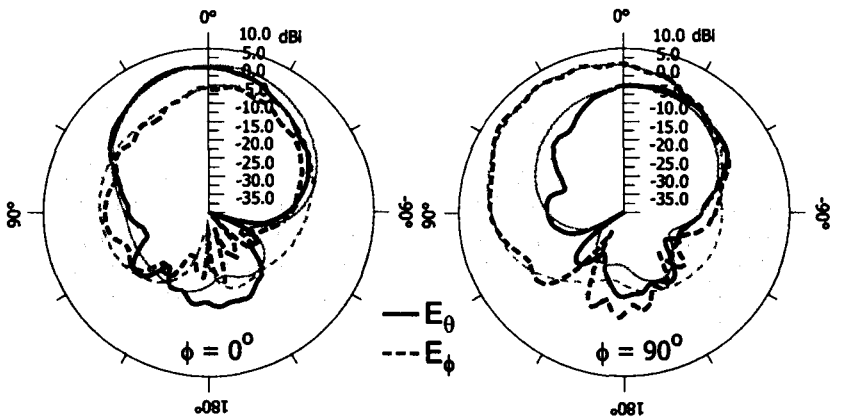

Figure A.5: Measured (black) and HFSS simulated (grey) radiation pattern of broadside configuration.

A.3 Cavity Model

The antenna discussed is modeled by an equivalent set of cavities. However, the antenna does not directly follow the operation of a rectangular patch (or other canonical shape [1]), so the resulting cavity model and radiating slots must be examined carefully because the geometry is being operating in higher order modes of the cavity. In [1, 5] it can be found that for low impedance lines (e.g., rectangular patches), the slot configuration for a linearly polarized radiator is constructed as two slots separated by the resonant length L. For each of these slots, there is a uniform electric field distribution with the appropriate polarization based on the fringing field distribution of the patch along the resonant length. The present analysis continues by representing the equivalent slots with magnetic current elements [1, 5]. This work deals primarily with the electric field representation of the radiating slots, so the magnetic currents will not be dealt with explicitly (although the analysis will be extended to this in the future).

A.3.1 Microstrip Patches and Radiators

To model the reconfigurable antenna as a resonant device, aspects of the cavity model are examined and discussed to justify the necessary assumptions associated with this analysis. For example, when modeling the rectangular microstrip geometry to higher degrees and/or for higher

order modes, the low impedance line presented by the rectangular geometry can be thought of as having four individual slots residing around the outer perimeter. Upon further investigation into the fundamental TM_{01} mode, it can be seen that the magnitude of the *secondary slots* (representing the fringing fields which support the modal - or sinusoidal - behavior along the sides of length L) is significantly smaller than the *primary slots* (along the width W which support a uniform electric field distribution). Along with the significantly smaller magnitude, the field distributions along these edges will experience destructive superposition in the far field at broadside due to the field polarization and spacing along these dimensions. For the reconfigurable antenna, the contributions from the slots associated with both of the characteristic dimensions (L and W) will differ from that of rectangular patch geometry. This is attributed to the reconfigurable antenna geometry which is: (1) wrapped into the square spiral geometry along the resonant length L and (2) a high impedance line of dimensions such that $W << L$.

A.3.2 Long Microstrip Radiators

Although different from the reconfigurable antenna in many aspects, the long microstrip radiator (LMR) discussed in [6] has interesting parallels in its geometry and operation. The LMR consists of a conducting strip wrapped around the axis of a cylinder (resonant along the width W), which is edge-fed by several microstrip lines parallel to the cylinder axis along the length L, similar to several rectangular patches contiguously connected. For the long microstrip radiator, the quasi-TEM transmission line mode transverse to L is excited using multiple edge-feeds per wavelength along L. This feeding technique is necessary to avoid exciting higher-order TM_{nm} modes, and will effectively radiate as if in the TM_{0m} mode (transverse to W in free space). In a cavity model analysis of this antenna, the primary radiating slots would reside along the perimeter length L (polarized perpendicular to L), similar to those of a very wide rectangular patch antenna.

A.3.3 High Impedance Long Microstrip Radiators

For the reconfigurable antenna, the quasi-TEM transmission line mode propagates on the line as in the long microstrip radiator; however, the probe (single) feed and narrow line suggest that several new assumptions be considered. This case is referred to as "high impedance" due to the resulting characteristic impedance of the narrow microstrip line width ($w<<h$) (as if it were supporting quasi-TEM propagation along L) being much higher than that of an equivalent rectangular patch. This will also orient the direct and fringing electric field distribution to be symmetric with respect to the center of the line width (Figure A.6). The existence of a single feed will also greatly influence the modal behavior of the antenna will support quasi-TEM propagation along the line length L which, when considered as a cavity, will resemble a TM_{0m} mode. In this configuration, the narrow line will experience the same phenomena as the patch (e.g. fringing fields, etc.), seen in Figure 6; however, the field structure will be modified as previously stated to the extent that the slots experiencing the modal distribution (transverse to L) become the primary radiating mechanism due their greater effective slot width, and the secondary slots are now ignored in a first order analysis, opposite to the case of a rectangular patch.

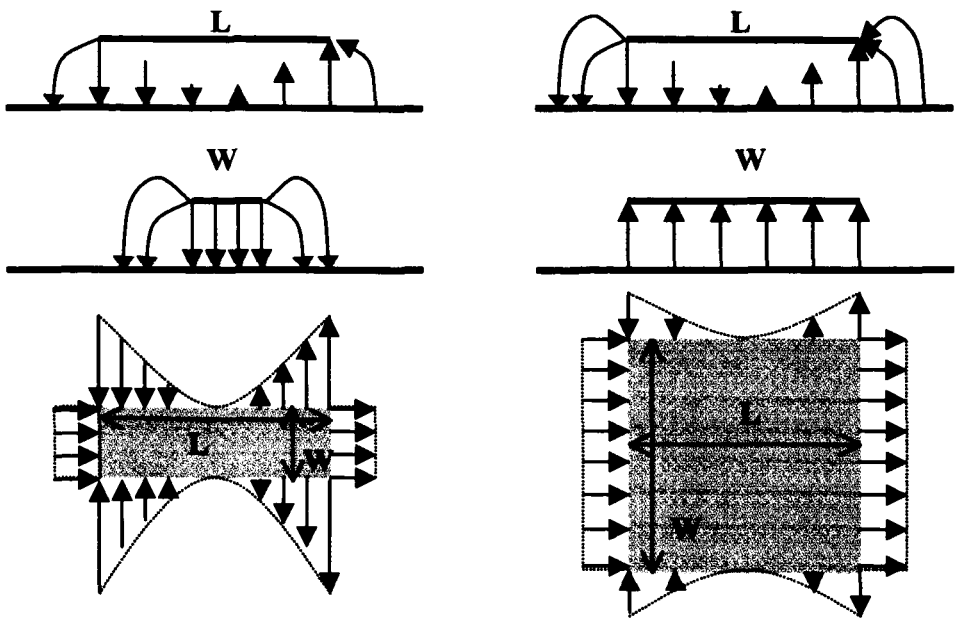

Figure A.6: Field distribution (top) and equivalent slots (bottom) for a 0.5 λ high impedance (left) and low impedance (right) microstrip line operating in the patch mode.

A.3.4 Cavity Model of the High Impedance Long Microstrip Radiator

The analysis begins first by constructing the appropriate cavities formed by all desired variations of the antenna and resulting electric field distributions. The geometric variations responsible for reconfiguration are created from the in-line switches discussed in Section A.2. Next, a set of appropriate wave functions is identified for all of the cavities, which can individually satisfy Laplace's Equation (Equation 1) and the appropriate local boundary conditions (Equation 2). Using these wave functions, the radiating mechanisms can be approximated using radiating slots and a basic description of the operation with respect to frequency can be attained.

$$\overline{\psi}\left(\nabla_t^2 + k^2\right) = 0 \text{ with } \overline{\psi} = \hat{z}\ \psi(x) \tag{1}$$

$$\frac{d\overline{\psi}(x)}{d\hat{n}} = 0 \text{ (magnetic) and } \hat{n}\cdot\overline{\psi}(x) = 0 \text{ (electric)} \tag{2}$$

To obtain the radiation characteristics of the antenna, all of the resonant behavior found from the cavity analysis are included and projected onto the ground plane of the antenna, as a properly phased and polarized pair (or pairs) of radiating slots. To analyze this behavior, a process using commercially available software has been explored which provides an approximation to the radiating slots in [1, 5]. The physical interpretation of these slots is the modal distribution of the fringing fields, or the equivalent vertical magnetic current distribution along the perimeter of the cavity. In conjunction with this, the microstrip structure can also provide a transmission line equivalent circuit, which incorporates the cavity and radiating slot impedance. However, the primary focus of this work will on the radiating properties of the antenna, and the impedance will be addressed in future work.

For this particular antenna, two further steps can also be made prior to analysis which aid in the modeling process. First, the antenna (a thin microstrip line) can be unwrapped into a linear geometry (or several geometries) to determine the wave function and later re-wrapped without significantly disturbing the wave function. Wherein, it is only along the unwrapped linear geometry that the modal behavior will develop and the resulting radiating slots will reside. Second, the probe feed used to excite the antenna can be considered a current source [1], which will resembles a short circuit (minimum electric potential) at the feed point in lieu of a forced (or hard) boundary condition. When the probe diameter and line width are comparable (the same dimension in this case), this will resemble an electric wall (boundary condition) in the cavity analysis, and force the modal electric field distribution to a minimum.

A.3.5 Endfire Configuration

The endfire configuration is examined first. With this geometry unwrapped counterclockwise, two cavities can be formed having the lengths L_1 and L_2, shown in Figure A.7. These represent the section of line from the grounding via to the open circuit and the length of line from the open circuit at e' to the probe feed, respectively. The first length L_1 is negligible in comparison to L_2 and λ_d, so contributions from this cavity can be neglected in the absence of a direct excitation for this section. The boundary conditions for this remaining cavity C_2 are magnetic at $x = 0$ where the open circuit resides (standing electric field is at a maximum), and electric at $x = x_1$ from the probe's appearance as a short circuit (standing electric field is at a minimum). The wave function which satisfies these two boundary conditions is given identified in Equation 3, with $L = L_2$.

$$\psi_m(x) = \cos(k_m x) \text{ with } k_m = \frac{(2m-1)\pi}{2L} \text{ and } m = 1,2,3,... \tag{3}$$

A.3.6 Broadside Configuration

For the broadside configuration, the geometry is unwrapped (Figure A.7) such that the probe fed section is opened up clockwise toward the negative x-axis and the section of line with the via to ground opened up counterclockwise toward the positive x-axis. The antenna can then be modeled as two cavities C_3 and C_4, representing the probe fed section of line of length L_3 and the parasitic section of line with the via to ground for length L_4. For the cavity C_3 the associated boundary conditions are magnetic at $x = 0$ (open circuit), and electric at $x = x_3$ (short circuit from probe), similar to the endfire configuration. The cavity C_4 is similar to the endfire configuration as well (reversed), with electric boundary conditions (the via to ground) at $x = x_2$ and magnetic (open circuit) at $x = x_4$. The resulting wave functions for these cavities are Equation 3 with $L = L_3$ and Equation 4 with $L = L_4$ for C_3 and C_4, respectively. Further, to facilitate a better impedance match with these capacitively coupled lines (coupling across the contiguous section f) the length L_3 is set slightly inductive (smaller in comparison to resonant length of L_4).

$$\psi_m(x) = \sin(k_m x) \text{ with } k_m = \frac{(2m-1)\pi}{2L} \text{ and } m = 1,2,3,... \tag{4}$$

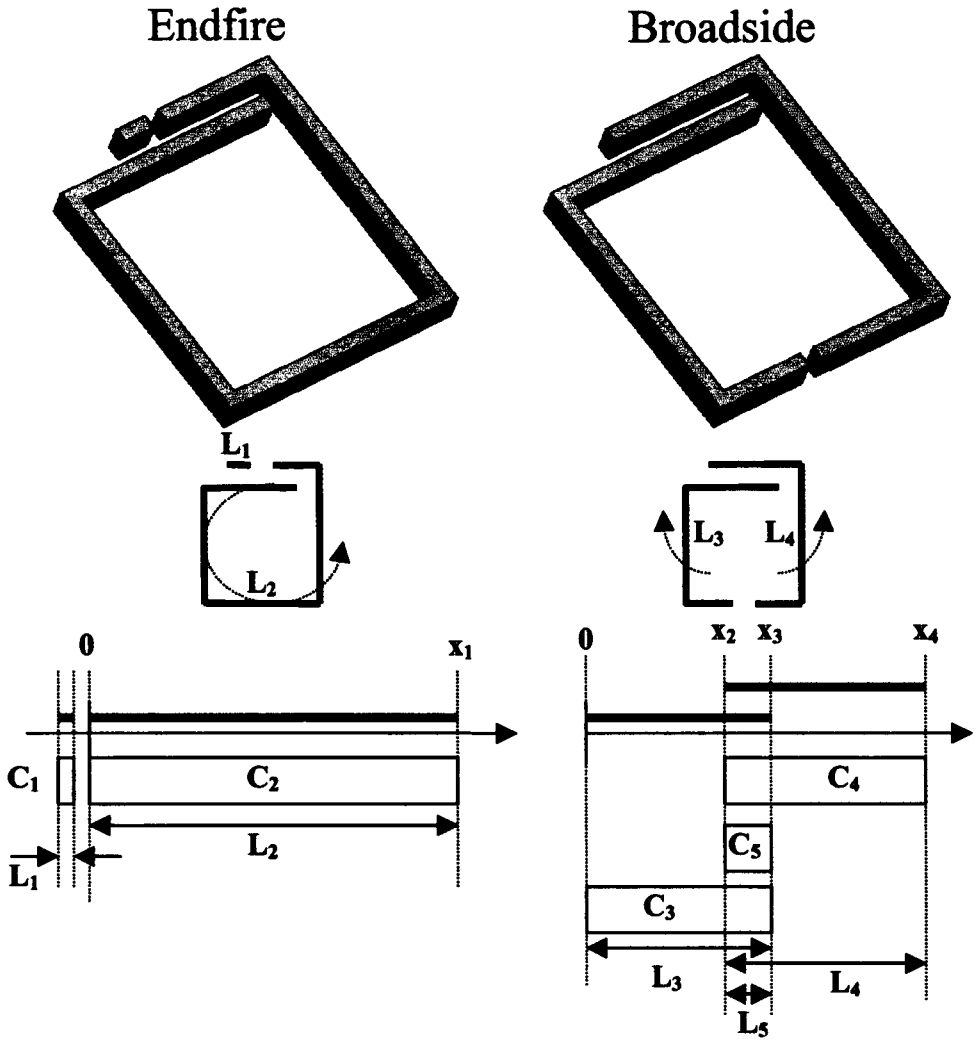

Figure A.7: Endfire (left) and broadside (right) reconfigurable radiation configurations. The resulting cavities (top) can be decomposed into similar sets of inner and outer slot geometries (middle), and unwound according to arrow direction (only the general shape is shown), which can be approximated by the cavity cross sections (bottom).

A.3.7 Cavity Representation of Coupling

A.3.7.1 Broadside Configuration

In the broadside configuration, the coupling across the contiguous spiral section (length *g*, separated by *s*) is essential to achieving the desired operation. The probe fed cavity C_3 is coupled to the parasitic cavity C_4 through the resonant behavior along the length f (Figure 7), which is set to ~ 0.5 λ_d. This behavior can also be modeled as a resonant structure in an analysis similar to [7]. This cavity is of length *g* and width *s*, and is formed by impressing the boundary conditions from the two neighboring cavities, creating electric walls of width *s* at x_3 and x_4. For these walls, it is assumed that the electric walls at x_2 and x_3 (especially the shorting via) will greatly influence the local field behavior across the distance *s* (~ 0.04 λ_d), which will also be in the vicinity of a voltage minima when the cavity is resonant. A magnetic wall on the surface of

the substrate completes the cavity geometry, and is created by assuming the electric field is primarily coupling in a differential mode across s and along g (from the probe fed section to the parasitic section). The wave function for this cavity is in Equation 5, with L = g; where coupling is greatest when this cavity shares resonance with the other two neighboring cavities, C_3 and C_4. This can be extended to include a phase delay δ (Equation 6) for the argument in Equation 4, associated with the delay of coupling onto the parasitic section.

$$\psi_m(x) = \sin(k_m x) \text{ with } k_m = \frac{m\pi}{L} \text{ and } m = 1,2,3...(all) \tag{5}$$

$$\delta = \frac{2\pi s}{\lambda_d} \tag{6}$$

A.3.7.2 Endfire Configuration

In the endfire configuration, the coupling from the contiguous portion of the spiral (length g, separated by distance s) can also be taken into account, but the effects are not as pronounced as in the broadside configuration. This is due to: (1) a voltage minima (in the cavity) at the location of the short when the cavity is resonant and (2) the isolation of the shorting via created by the open circuit at e', which perturbs the cavity and prevents the resonant coupling behavior seen in the broadside configuration. However, some interaction will occur from differential mode coupling and can be accounted for by superimposing a second wave function in the cavity (identical to Equation 3) with the additional phase delay δ (Eq. 6) in the argument. Without the resonant coupling, the effect of the superimposed wave function has a decreased magnitude and will be minimal. In a transient analysis, this interaction is responsible for the ringing this geometry experiences, along with the higher Q (or lower bandwidth) similar to a spiral inductor.

A.3.8 Reconfigured Frequency

After the appropriate wave functions have been determined, the resonant frequencies of the cavity can be calculated. Using the wave number k_m found in the previous sections, an approximate resonant frequency can be calculated using Eq. 7, where ε_d is the dielectric permittivity. Using this process in reverse (identical to the process determining rectangular patch dimensions), one can easily obtain approximate dimensions of reconfigurable antennas for other substrates and operating frequencies. A continuation of this topic will be addressed in future work.

$$k_m = \frac{(2m-1)\pi}{2L} = 2\pi f_m \sqrt{\mu\varepsilon_d} \tag{7}$$

A.4 Radiating Slots: Representation and Evaluation

To validate the cavity model of the radiation reconfigurable antenna, a method using commercially available software has been used. It provides approximations to the physical mechanisms of the cavity model that are responsible for the radiation behavior. In this approach,

the radiating slots used to represent the fringing electric fields are modeled using features common to many full wave electromagnetic solvers. To model the slots directly, the representative slot areas residing at the appropriate physical locations on the ground plane can be excited as if they were radiating apertures. The polarization, phase and magnitude of these apertures can be tailored within the program, and may also incorporate local boundary conditions to force the electric field distribution in the slot to a modal or non-modal profile. While this approach provides useful information about the radiation features without including all of the geometric features, it does not accurately model the impedance due to the ambiguity of the excitation with regard to a specific feed location.

For this work, HFSS 9.1 has been used to model the radiating slots. Within the framework of the software, the radiating slots of the microstrip antenna can be modeled as "wave port" excitations, located where the slots would be projected onto the ground plane of the antenna geometry. To accommodate this excitation, the ground plane of the antenna must first be extruded into a volumetric element of finite conductivity (copper was used for this study) and nominal thickness below the substrate. For all of the results obtained in this work, the ground planes have been given a thickness of 0.25 mm. This must be done as to not allow energy to enter or exit through the back of the wave port (a passive, 1 port device). Next, the planar geometries of the radiation slots are created on the interface between the substrate and ground plane. These slots are then excited as a wave port and polarized accordingly. In this orientation, the boundary conditions around the port geometry will be electric by default due to its location on the surface of the conductive slab. If a magnetic boundary condition is required (as is the case with an open circuited line), a nominally small area (or appropriate vertex) can be created and assigned as such, along the desired dimensions tangent to the polarization of the slot.

A.4.1 Example: Rectangular Microstrip Patch

To evaluate the wave port representation of the radiating slots, a probe fed rectangular microstrip patch antenna designed to operate at 5.775 GHz (L = 8.2 mm and W = 14 mm) has been modeled and fabricated on a finite ground plane and substrate (Duroid 6006, $\varepsilon_r = 6.15$ and h = 2.54 mm with probe dimensions same as reconfigurable antenna). To approximate the radiating slots, the patch is replaced by two slots (wave ports) with the appropriate orientation, spacing, and polarization determined by the patch dimensions and cavity model. For the patch, the field distribution within the slot is approximately uniform, so magnetic boundary conditions are enforced at the opposing ends of each slot. The layout for both the patch and the slots can be seen in Figure A.8.

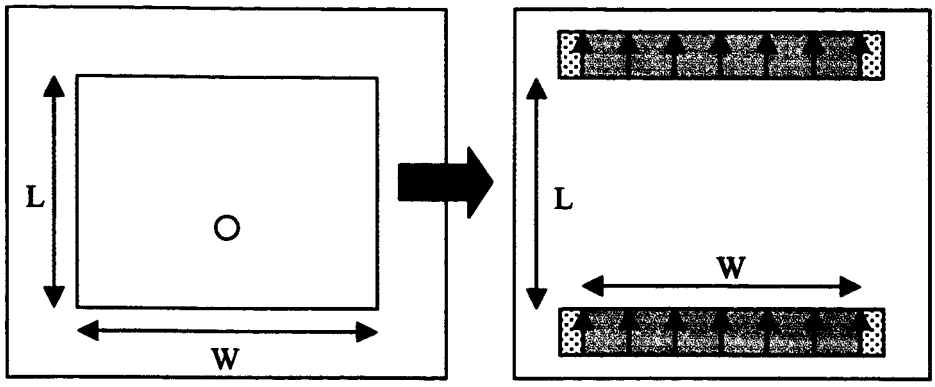

Figure A.8: Patch antenna (left) and equivalent radiating slot model using wave ports in HFSS (right). The ground plane is light gray, the slot (wave port) is dark gray, hatched areas outside the slot represent magnetic boundary conditions, and arrows indicate slot polarization.

A.4.2 Results: Rectangular Microstrip Patch

Measured and simulated radiation patterns from this patch can be seen in FigureA.9. Examination of these patterns demonstrates the wave port's ability to provide a good representation of the physical radiating mechanism associated with microstrip antenna patch-mode. It should be noted that effects from the finite ground plane are present with the wave port approximation, shown by the development of back-plane radiation that closely matches the measured antenna behavior. Using these results as an indication of the accuracy which can be obtained from the model's approximation, the reconfigurable antenna can be simulated and the results can be interpreted.

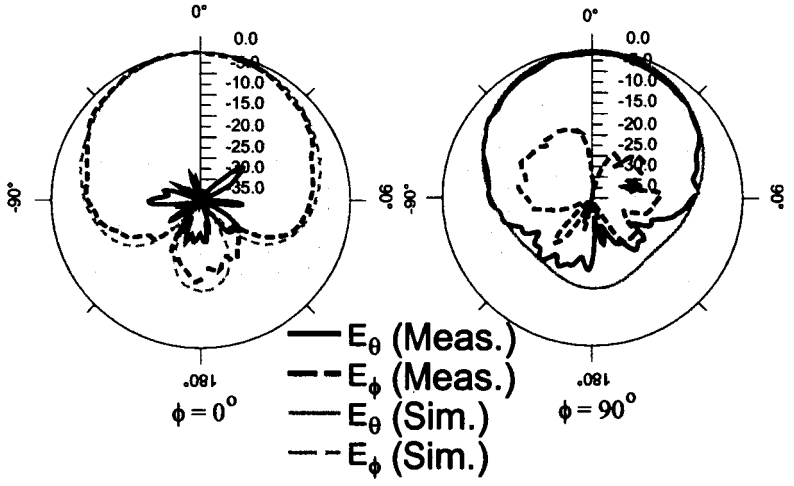

Figure A.9: Measured (black) and simulated radiating slot (gray) radiation patterns for the microstrip patch example.

A.4.3 Reconfigured Radiating Slots

For the radiation reconfigurable antenna discussed in this work, an approximate radiating slot distribution can also be obtained according to the description in Section A.3. The polarization and phasing of these slots must be representative of the physical electric field distribution, so special attention must be given to the individual slots to ensure the accuracy of the model. After

creating these slot pairs transverse to the length of the line segment(s) that bound the cavity or cavities, the proper boundary conditions are created along the end of the slots according to the cavity analysis. For these full-length slots, the modal distribution will develop according to the imposed boundary conditions and will be used in the following sections to model the antenna's radiation. The geometries that have been simulated to approximate the radiating slots can be seen in Figure A.10 for the previous patch example and the following section on the reconfigurable antenna.

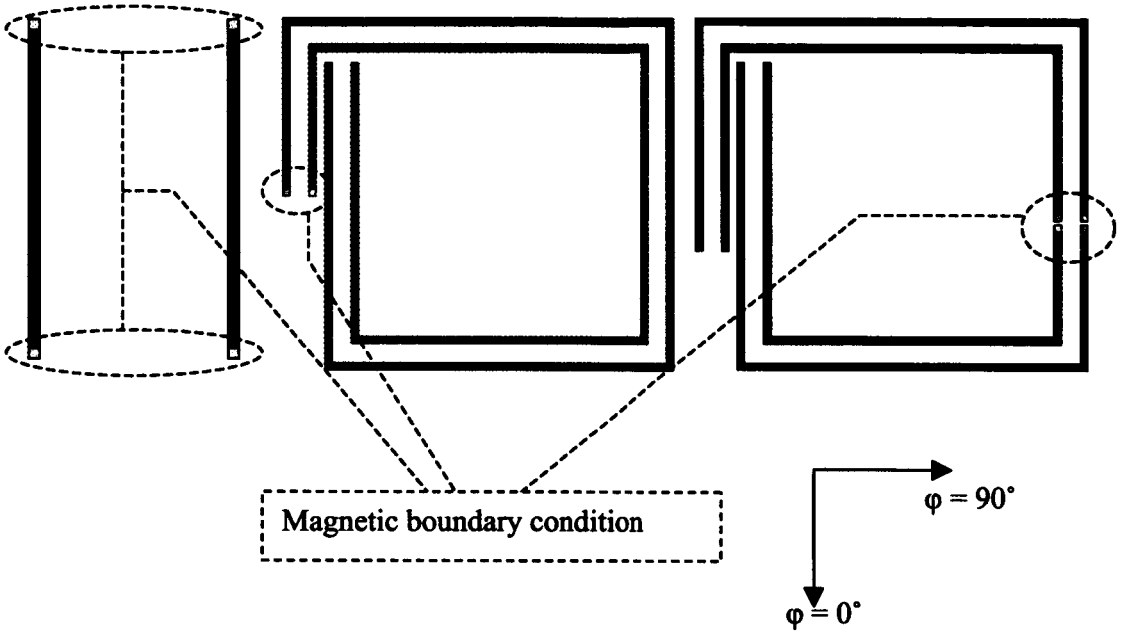

Figure A.10: Slot geometries for the simulated patch (left), endfire (middle), and broadside (right) to represent the radiating slots obtained from the cavity model. Individual slots are black, with magnetic boundary conditions in gray (and circled).

A.5 Measured and Simulated Radiation Characteristics

Measured and simulated results for the reconfigurable antenna are presented in Figures A.11 and A.12. At the corresponding frequency (~ 6.9 GHz) for these modes, both configurations will exhibit resonant behavior and the impedance will be dominated by the radiation resistance of the antenna. In both configurations, the measured and simulated radiation patterns have been normalized independently and show good agreement between the simulated equivalent slots and the measured results. In Figure A.11, the results for the endfire configuration show the development of nulls in the broadside direction that are very close in depth and direction. In the dominant polarization, E_θ, the agreement is very close. In the orthogonal polarization, E_φ, the level of agreement between the simulated and measured is not as high, but the general characteristics and shaping of the radiation is similar. This effect on the non-dominant polarization can be attributed to the idealistic conditions of the two parallel slots with opposite tangential polarizations, which does not completely model the interaction of the fringing fields. Specifically, the superposition of the fields with ideal slots effectively cancels each other better in the far field, more so than the fabricated antenna. Additionally, corner effects present in the real (measured) antenna may not be fully captured in this model of the slots.

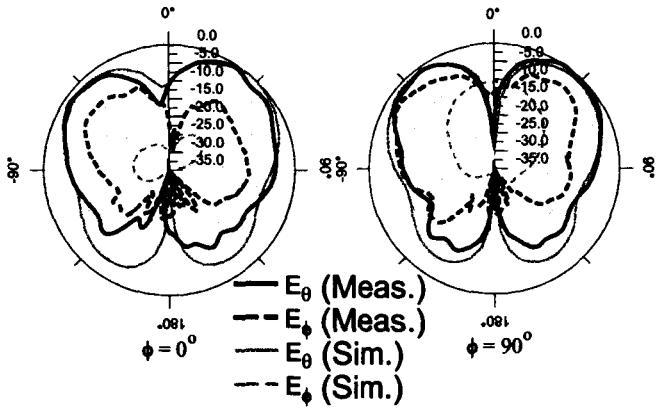

Figure A.11: Measured (black) and simulated radiating slot (gray) radiation patterns for the endfire configuration.

In the broadside configuration (Figure A.12), the general behavior of the radiating slots accurately describes the measured performance antenna. In this configuration the electric field distribution along the line is shifted by 0.25 λ_d (with respect to the endfire configuration) due to the shorted section that creates maxima located closer to the corners of the antenna, providing a slight imbalance in the field distribution between the inner and outer apertures. This effectively keeps the opposing polarizations from completely canceling each other (as in the case of the endfire configuration) and creates the broadside radiation characteristics, as well as the tilt in the main beam due to slight offsets in the antenna's modal distribution around the corners..

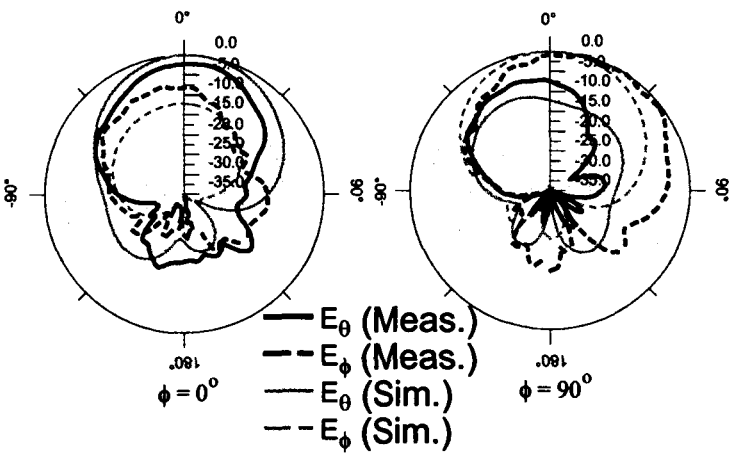

Figure A.12: Measured (black) and simulated radiating slot (gray) radiation patterns for the broadside configuration.

A.6 Conclusions on Cavity Model for Reconfigurable Antenna

In the preceding sections we applied the cavity model originally developed for rectangular patch antennas to a thin line (W << L) spiral microstrip radiation and frequency reconfigurable antenna. A method for approximating the radiation of the cavity model for complex geometries has also been successfully explored using commercially available software, and has been used to

verify the operation of the antenna in a higher order patch-mode. Future work will focus on the development of design equations based on the fundamental cavity relationships obtained from this analysis.

A.7 References for Section A

[1] Y. T. Lo, D. Solomon, and W. F. Richards, "Theory and experiment on microstrip antennas," *IEEE Transactions on Antennas and Propagation,* vol. 27, no. 2, pp. 137 – 145, March 1979.

[2] G. H. Huff, J. Feng, and J. T. Bernhard, "Small array of boresight to endfire radiation reconfigurable antennas," *Proc. 2003 Antenna Applications Symposium*, Allerton Park, Monticello, Illinois, 2003, pp. 147-161.

[3] G. H. Huff, J. Feng, S. Zhang, J. T. Bernhard, "A novel radiation pattern and frequency reconfigurable single turn square spiral antenna," *IEEE Microwave and Wireless Components Letters*, vol. 13, no. 2, pp. 57-60, Feb. 2003.

[4] G. H. Huff, J. Feng, S. Zhang, and J. T. Bernhard, "Directional reconfigurable antennas on laptop computers: simulation, measurement, and evaluation of candidate integration positions." *IEEE Transactions on Antennas and Propagation*, vol. 52, pp. 3220-3227, December 2004.

[5] W. Richards, Y. T. Lo, and D. Harrison, "An improved theory for microstrip antennas and applications," *IEEE Transactions on Antennas and Propagation*, vol. 29, no. 1, pp. 38-46, Nov. 1981.

[6] J. Gomez-Tagle and C.G. Christodoulou, "Extended cavity model analysis of stacked microstrip ring antennas," *IEEE Transactions on Antennas and Propagation*, vol. 45, no. 11, pp. 1626-1635, Nov. 1997.

[7] H. Himdi, J. P. Daniel, and C. Terret, "Analysis of aperture-coupled microstrip antenna using cavity method," *Electronics Letters*, vol. 25, no. 6, pp. 391 – 392, March 1989.

[8] R. E. Munson, "Conformal microstrip antennas and microstrip phased arrays," *IEEE Transactions on Antennas and Propagation*, vol. 22, pp. 74-78, Jan. 1974.

[9] A. Derneryd, "Linearly polarized microstrip antennas," *IEEE Transactions on Antennas and Propagation*, vol. 24, no. 6, pp. 846-851, Nov. 1976.

[10] A. Derneryd and A. Lind, "Extended analysis of rectangular microstrip resonator antennas," *IEEE Transactions on Antennas and Propagation*, vol. 27, no. 6, pp. 846-849, Nov. 1979.

[11] D. Chang, "Analytical theory of an unloaded rectangular microstrip patch," *IEEE Transactions on Antennas and Propagation*, vol. 29, no. 1, pp. 54-62, Nov. 1981.

[12] S. Mutlu and M. I. Aksun, "Hybrid model for probe-fed rectangular microstrip antennas with shorting pins," *2000 IEEE Antennas and Propagation Society International Symposium*, vol. 3, 16-21 pp. 1448 -1451, July 2000.

B. Performance of antenna in array configurations for broadside and endfire operation

For the radiation reconfigurable antenna discussed in this project, the pattern may be switched between broadside and endfire over a common impedance bandwidth with two surface mount in-line reflective switches. Using the reconfigured radiation characteristics of the antenna as an extra degree of freedom in an array, the performance and element behavior is now studied in an array setting.

B.1 Reconfigurable Radiation and Array Factor

To fully incorporate the reconfigurable radiation properties as an extra degree of freedom in the array, the superposition of the array factor and the two reconfigured single element patterns were examined. To do so, the array spacing and phasing is examined for two possible array configurations in an effort to best recover the single element functionality (with the added benefits of the array). Specifically, the array spacing (d_x and d_y) and phasing (δ_x and δ_y) is examined for 'static' and 'dynamic' array factors, each providing the possible conditions needed to recover the desired functionality. To qualitatively examine the performance of the two array settings, the array factor for each array configuration is calculated and superposition with the single element patterns. The results are used to evaluate and predict the conditions for experimental work.

B.1.1 Static Array Factor

The static array factor is examined first, and effectively imposes the element patterns to dictate the peak and null directions of the main beam. In this setting, the array factor simultaneously provides major lobes in both the broadside and endfire directions. This setting is referred to as the static array factor since it is un-phased and the array factor does not change throughout the operation of the array. To achieve this behavior from the array, the element spacing is set to a full wavelength ($d_x = d_y = \lambda_{RR}$) at the center frequency of the shared impedance bandwidth and feeding all elements in-phase. For superposition at f = 6.9 GHz, this requires setting $d_x = d_y =$ 43.18 mm and $\delta_x = \delta_y = 0^\circ$. Prior to further examination, several obvious trade-offs are considered which can influence the behavior of the array. The most significant of these trade-offs is the decrease in complexity (no phasing) and density with the full wavelength spacing, with poor pattern control due to the interaction of grating lobes (from spacing) and non-ideal pattern characteristics of the single element as well as lower possible gain from decreasing the array density (sparse array).

B.1.2 Dynamic Array Factor

An array factor that compliments the two different reconfigured radiation patterns is examined next. In general, this is essentially examines the worst case scenario when steering the main beam of the array from broadside to endfire. In this setting, the element spacing is set to a half-wavelength ($d_x = d_y = 0.5\lambda_{RR}$) at the center frequency of the shared impedance bandwidth and all elements are progressively phased 180° in either the x-direction or y-direction while those in the orthogonal direction are fed in phase. For superposition, this requires setting $d_x = d_y = 21.74$ mm and setting $\delta_x = 180^\circ$ with $\delta_y = 0^\circ$ or $\delta_x = 0^\circ$ with $\delta_y = 180^\circ$. This array factor changes according to the element behavior, so it referred to as the dynamic array factor. In this configuration, several trade-offs are also considered. Specifically, the major trade-off is between the higher gain (more dense array) and improved pattern behavior (decreased grating lobes) for the effects

from mutual coupling between the elements resulting from the close (< 0.1 λ_{RR} in both x- and y-directions) inter-element spacing.

B.1.3 Superposition Results

The resulting 2-element (N = 2) linear array factors for both static and dynamic configurations are shown in Figure B.1. Superposition is used next to approximate the performance of the small array and obtain a qualitative measure of the reconfigurable radiation behavior in the array. To do so, the measured single element patterns are superimposed with the 4-element (N = 4) linear array factors. For brevity, only the radiation patterns for the $\varphi = 0^\circ$ elevation cut-plane (for both static and dynamic cases) are shown in Figure B.2 for the endfire configuration and Figure B.3 for the broadside configuration (each plot contains both polarizations for both array settings). Behavior in the other primary planes of interest follows the results of the plane shown closely, and do not show any pattern anomalies or unexpected behavior. Examination of these plots demonstrates that the two different element patterns do not sufficiently control/facilitate the static array factor. These results indicate that the overall reconfigurable behavior between the endfire and broadside configurations is indiscernible in this setting. This behavior (undesirable lobes in the static array factor setting) is derived from the superposition the grating lobes and the non-ideal pattern characteristics of the single antenna element. In contrast, the dynamic array factor has acceptable pattern behavior that is well defined, having little in the way of undesirable side lobes and nulls. Interpreting these results, it is evident that the dynamic array factor offers the best possible performance for the array.

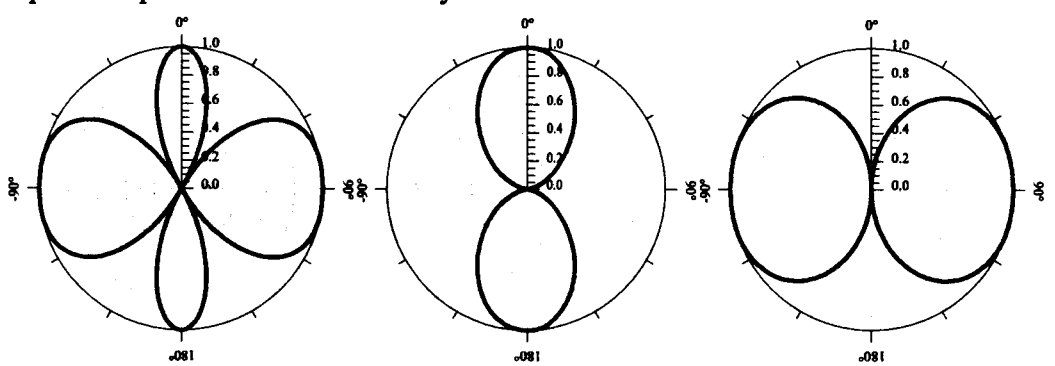

Figure B.1: Two element array factors used to determine the operational characteristics of the antenna in an array setting; (left) configuration 1 uses full wavelength spacing and is un-phased, (middle) and (right) configuration 2 uses half-wavelength spacing and is un-phased and progressively phased 180 degrees for the broadside and endfire configurations respectively.

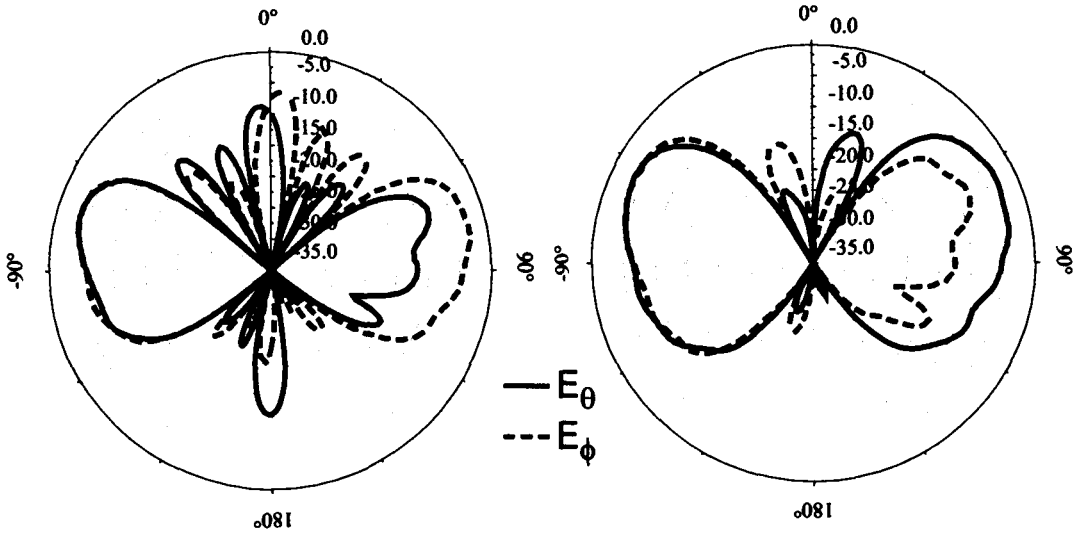

Figure B.2: Calculated elevation radiation ($\varphi = 0°$) patterns for the endfire configuration comparison of the static (left) and dynamic (right) array settings.

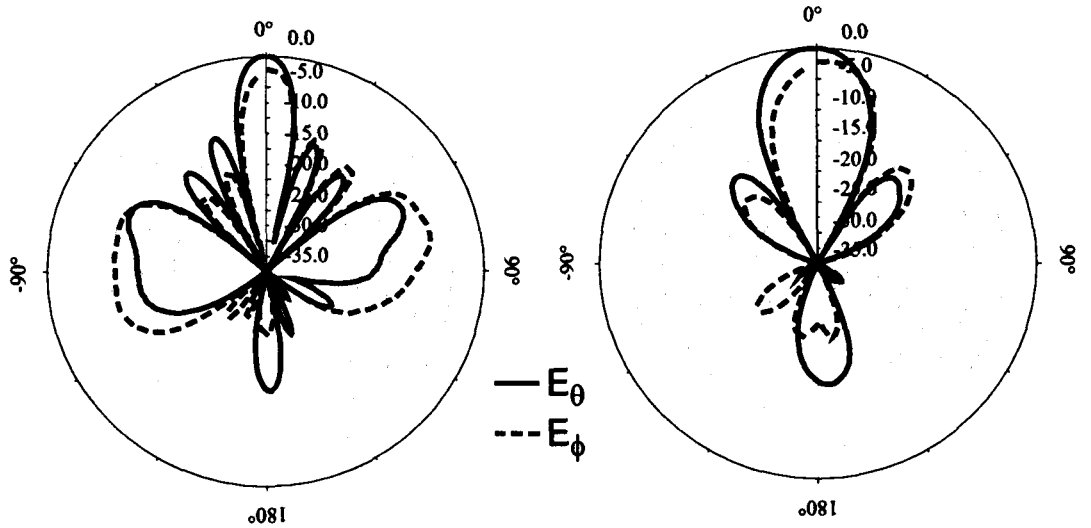

Figure B.3: Calculated elevation ($\varphi = 0°$) radiation patterns for the broadside configuration comparison of the static (left) and dynamic (right) array settings.

B.2 Two Small Arrays of Radiation Reconfiguration Elements

The behavior (calculated in the previous section) of 2×2 and 4×4 arrays of radiation reconfigurable antennas is examined next. These two array sizes are chosen for their size, symmetry, and the conditions that the 2×2 array has no interior elements and 4x4 array contain interior elements as well as 13 attainable subsets of the 2×2 (one of these subsets completely composed of interior elements). Dimensionally, the spacing in both fabricated arrays is 21.8 mm (~0.5λ) in both the x-direction and y-direction. Using this spacing, the inter-element distances in the x-direction and y-direction are 3.8 mm (.087λ) and 1.575 mm (.036λ), respectively. To complete the array factor for each configuration, two separate phasing schemes are used in the

array to recover endfire or broadside radiation. These two phasing schemes involve feeding all elements in phase while the antennas are in the broadside configuration and feeding the endfire configuration with progressive phase reversal along the x-direction or y-direction ($\delta_x = 180^\circ$ and $\delta_y = 0^\circ$ or $\delta_x = 0^\circ$ and $\delta_y = 180^\circ$ in the xz-plane or yz-plane respectively).

B.3 Experimental Results

For the two fabricated arrays of radiation reconfigurable antennas (Figure B.4), the measured radiation patterns in the two principle elevation planes, individual element VSWR bandwidths, and inter-element coupling are provided. To measure these arrays, components of the power division and phase shifting networks were both built and purchased commercially. In the endfire configuration the test setup consisted of the following components (in connective order): 1 Anaren 41130 2-way power splitters (2 – 18 GHz), 2 Anaren 41730 8-way power splitters (2 – 18 GHz), 16 RFCoax 3.0-inch low loss semi-rigid cables, 16 channel delay line board (fabricated) with four 4-channel progressive phase shifts (0°, 180°, 360°, 520°), and 16 MiniBend 15.0-inch low-loss coaxial cables. For the endfire configuration, the progressive phasing was applied sequentially in the rows or columns of the array to achieve the phase distribution in the desired plane. For the broadside configuration, the phase shifting network and RFCoax connections were omitted. In the anechoic chamber, this entire assembly was shielded by a metallic box clad in microwave absorbent material to minimize interference with the radiation pattern measurements. To measure the inter-element coupling in both arrays (in both configurations) with the 2-port VNA, a single element was chosen to remain the active element (i.e., port 1) and a second element was connected (i.e., port 2) while all others were terminated in the characteristic impedance (50Ω). The resulting transmission was then measured, and the process was repeated for the remaining elements in the array. To generate a qualitative display of the data, a method similar to [1] was used, and the interpolated contour of the inter-element coupling is given in dB for the respective plots.

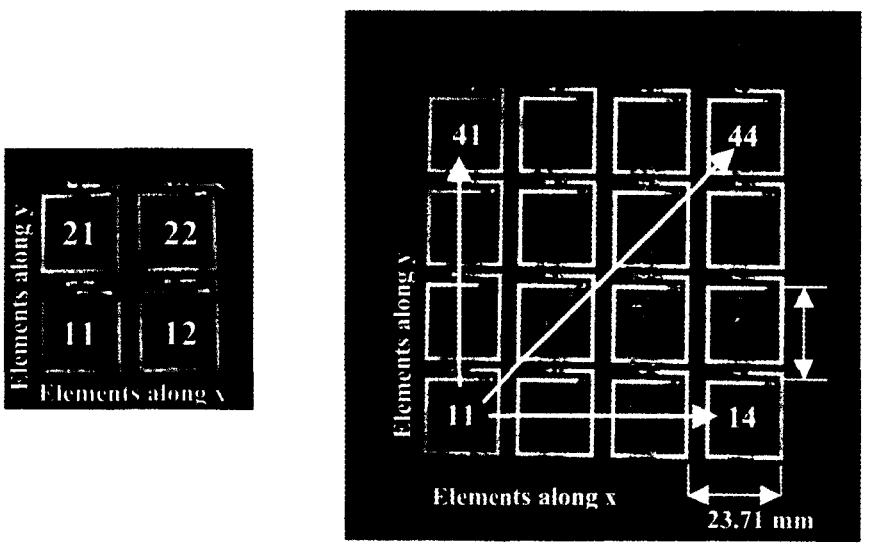

Figure B.4: Fabricated 2 × 2 (left) and 4 × 4 (right) arrays of radiation reconfigurable antennas. Element numbering begins in the bottom left corner of the array for both row (x) and column (y) directions.

B.3.1 2 x 2 Array

B.3.1.1 Shared VSWR Bandwidth

For the 2×2 array, the measured VSWR of the individual array elements in both the endfire and broadside configurations are shown in Figure B.5. In this array, the 2:1 VSWR bandwidth was increased uniformly in both configurations, up to 318 MHz for the broadside configuration and 115 MHz for the endfire configuration. In total, the resulting common impedance bandwidth is slightly broadened in the array to 98.0 MHz (1.43% BW) and has a shifted center frequency of 6.845 GHz. Results for VSWR are tabulated in Table B.1, which include the single element values for comparison.

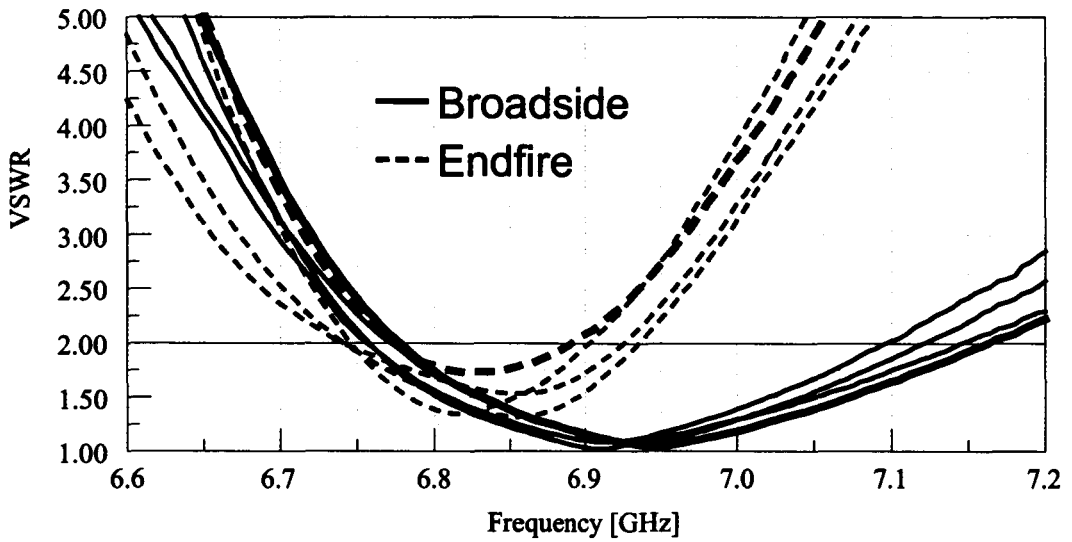

Figure B.5: Measured VSWR of 2 ×2 array; broadside (solid) and endfire (dashed).

Table B.1: Comparison of center frequency and VSWR bandwidth for the single element, 2×2 array, and 4×4 array (including trends).

	Broadside		Endfire	
	Single Element			
f_c	6.88 GHz		f_c = 6.88 GHz	
BW	170 MHz		90 MHz	
	2×2 Array			
f_c	f_c = 6.88 GHz		f_c = 6.88 GHz	
BW	318 MHz		115 MHz	
	4×4 Array			
Group	A	B	C	D
Array Elements	rows 1 and 4	rows 2 and 3	row 4, 12	rows 1, 2, 3, 11, 13, and 14
f_c	6.94 GHz	7.03 GHz	6.9 GHz	6.88 GHz
BW	250 MHz	318 MHz	100 MHz	134 MHz

B.3.1.2 Reconfigured Radiation

Measured radiation patterns for the broadside and endfire configurations are shown in Figures 10, 11 and 12 for the 2x2 array. The broadside configuration (Figure B.6) is linearly polarized with nominal side lobe and cross-polarization levels, achieving an overall gain of 12.4 dBi (E_θ in xz-plane and E_φ in yz-plane); representing the maximum gain of both configurations. The endfire configuration, when phasing independently along either the xz-plane (Figure B.7) or yz-plane (Figure B.8), maintains well defined linearly polarized (E_θ) endfire radiation characteristics while effectively nulling out radiation in the non-phased elevation plane. Effects of the finite ground plane dimensions can be seen in the behavior of the endfire radiation patterns for this configuration. For each of the endfire phasing scenarios, the maximum radiation occurs at an elevated angle away from true endfire ($\theta = 90°$), at approximately $\theta = 50°$ (mean) with a gain of 9.52 dBi and 9.42 dBi, respectively. This behavior is similar to a monopole over a finite ground plane, and is a result of both edge diffraction and truncation of the fringing electric field distribution. The element was further examined using several ground plane dimensions and an infinite ground plane approximation, at which point it was found that the pattern squinting diminishes with increasing ground dimensions.

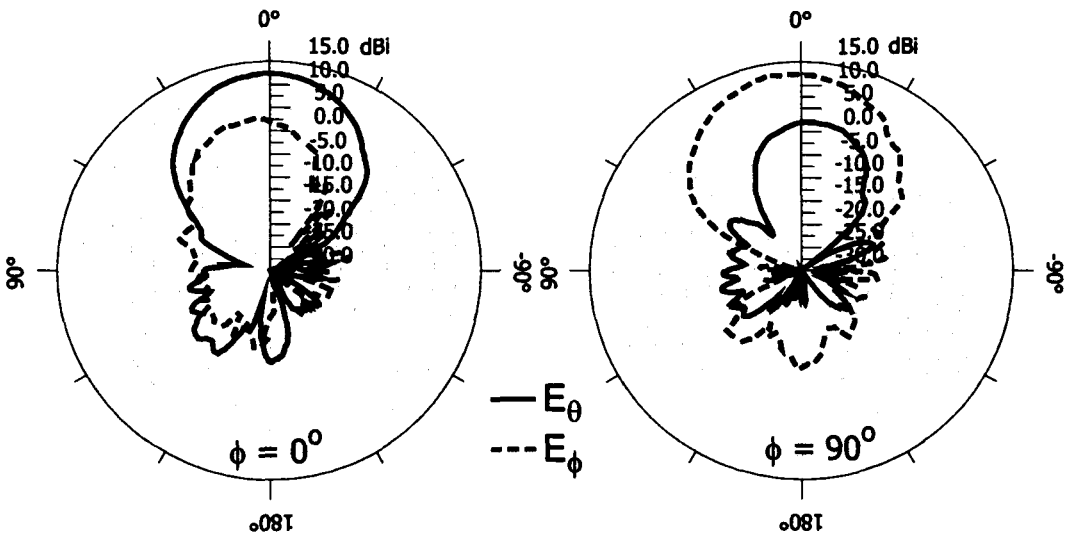

Figure B.6. Measured elevation radiation patterns for the 2 × 2 array in broadside configuration.

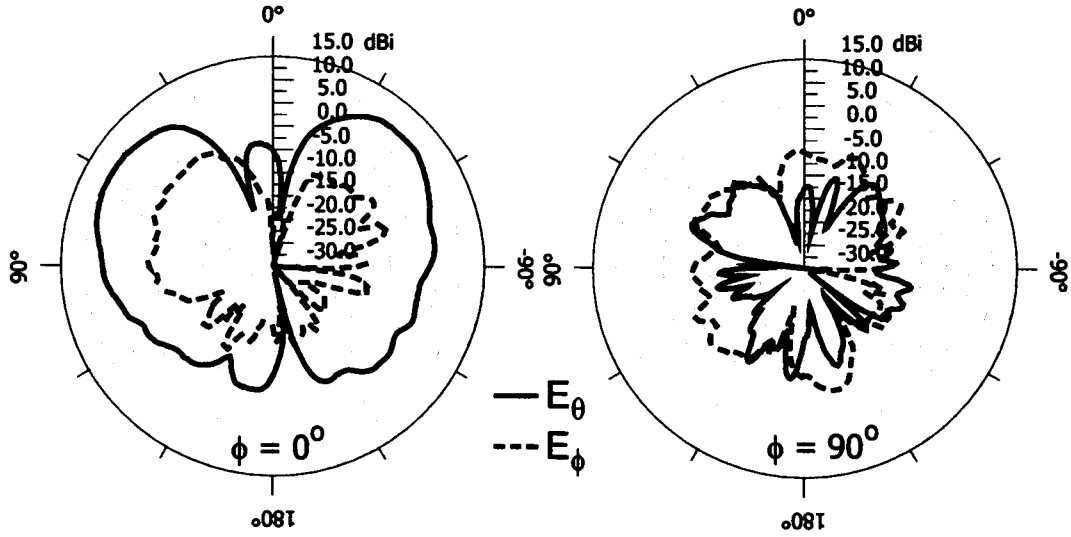

Figure B.7: Measured elevation radiation pattern for the 2 × 2 array in the endfire configuration, phase-reversal in xz-plane ($\varphi = 0°$), in-phase in yz-plane($\varphi = 90°$).

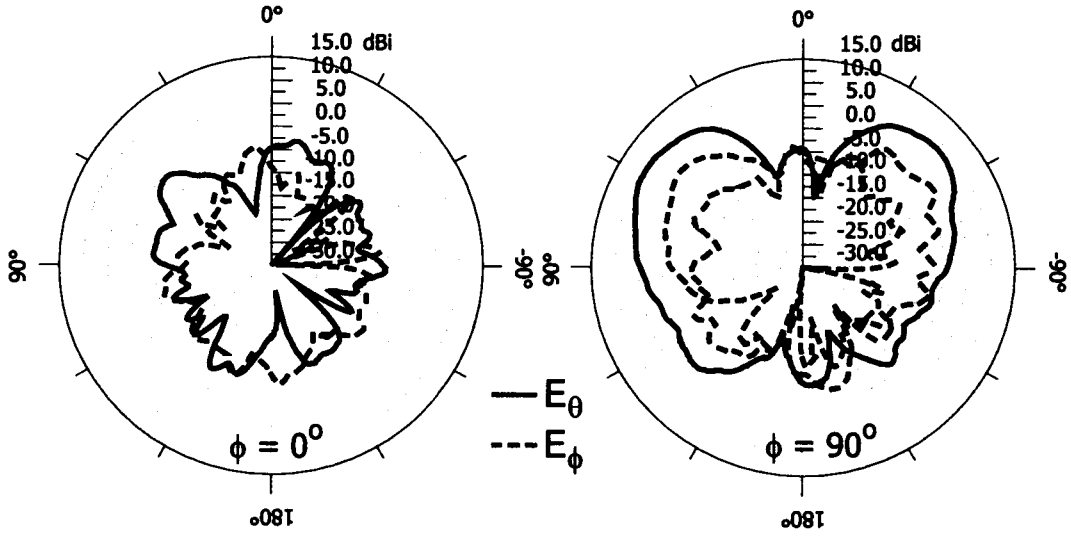

Figure B.8: Measured elevation radiation pattern for the 2 × 2 array in the endfire configuration, phase-reversal in yz-plane ($\varphi = 0°$), in-phase in xz-plane($\varphi = 90°$).

B.3.1.3 Mutual Coupling

The inter-element coupling in the 2×2 array is shown in Figure B.9 for both configurations (endfire is left, broadside is right). The active element is representative of the sub-plot position as it relates to the array element numbering in Figure B.4 (i.e., element 22 element is located in the upper right quadrant). The shifting and expansion/compression of element VSWR bandwidths are attributed to this mutual coupling. In this array, these effects are minimal and no major groupings or trends were observed; however, examination of these two plots demonstrates the asymmetry and geometric dissimilarities between the two configurations.

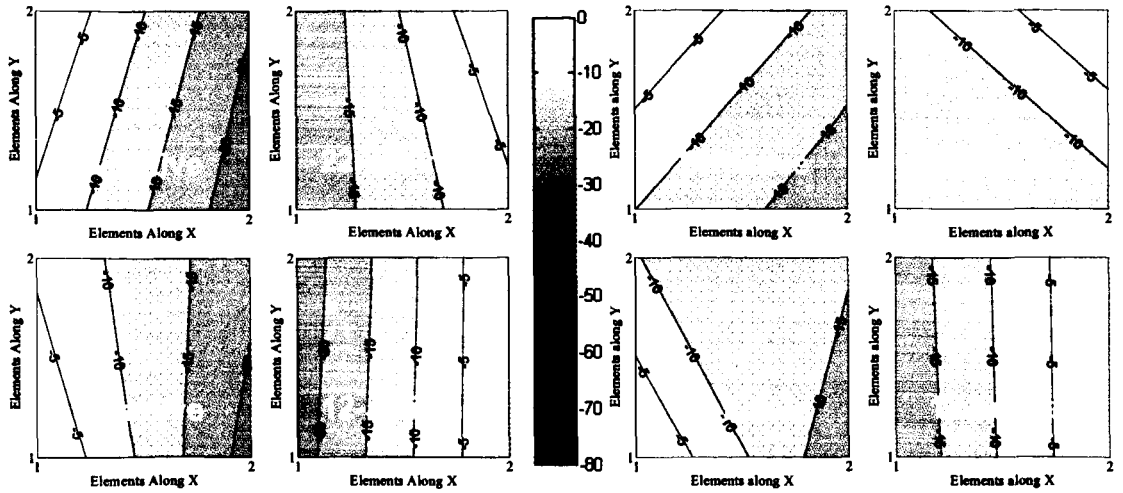

Figure B.9: Measured mutual coupling in the 2 × 2 array of endfire (left) and broadside (right) configurations.

B.3.2 4 × 4 Array

B.3.2.1 Shared VSWR Bandwidth

The measured VSWR of the 4×4 array elements is shown in Figure B.10 (broadside on top and endfire on bottom); with the grouping of similar trends A, B, C, and D (limiting cases in bold). This behavior is summarized in Table 1 with the single element and 2×2 array results for comparison. With the addition of interior elements (unlike the 2×2 array), trends were observed in both configurations which correlate to the position of the element in the array (in each configuration); specifically the element's row. These trends are especially evident in the broadside configuration, in which the coupling across the contiguous section plays a key role in the operation of the individual elements. In this configuration the close element spacing provides alternate avenues of coupling to neighboring elements and results in an increased bandwidth. In the broadside configuration, the two major trends occurred in the inner (group A) and outer rows (group B), which have increased bandwidths of 318 MHz and 250 MHz, respectively. For the endfire configuration, group C (rows 2, 3, and 4) increased to 134 MHz; while group D (row 1) only increased to 100 MHz. In total, the common impedance bandwidth is slightly decreased to 77.0 MHz due to the shifting of the endfire impedance bandwidth.

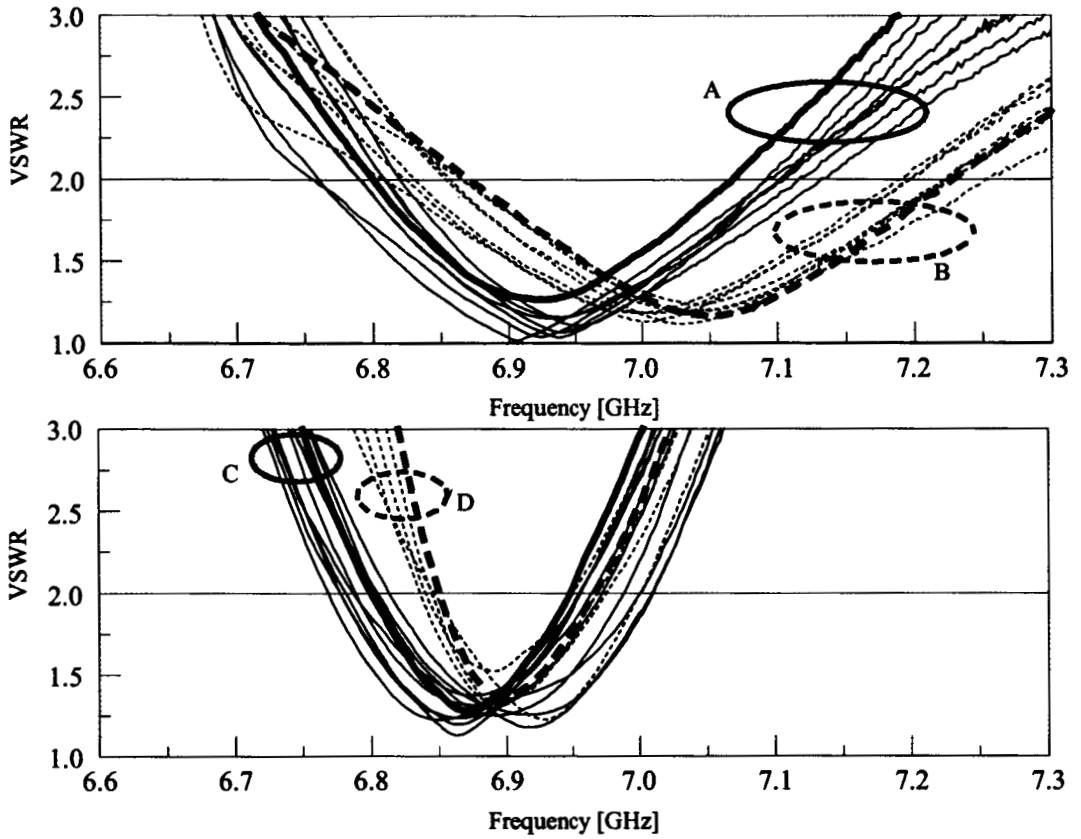

Figure B.10: Measured VSWR of 4 × 4 array in the broadside (top) and endfire (bottom). Grouping of elements (A, B, C, D, dotted, and dashed) is described in Table 3.

B.3.2.2 Reconfigured Radiation

The measured radiation patterns for the broadside and endfire configurations are shown in Figures B.11, B.12, and B.13. The broadside configuration (Figure B.11) remains linearly polarized with nominal side lobe and cross-polarization levels, and an overall gain (E_θ in xz-plane and E_φ in yz-plane) of 18.2 dBi (the maximum radiation occurs in this configuration). The endfire configuration, when phasing independently along either the xz-plane (Figure B.12) or yz-plane (Figure B.13), is linearly polarized (E_θ) endfire radiation characteristics and effectively nulls out radiation in the non-phased elevation plane. There exists abnormalities (decreased gain and pattern quality) when phasing in the yz-plane (Figure B.13) which are attributed to mutual coupling (examined next). This result corresponds to the variations in impedance bandwidth between the rows (along the yz-plane), where the individual elements are behaving differently. Effects of the finite ground plane dimensions are also observed in the radiation patterns for the endfire configuration in both phasing scenarios. For each of these (Figure B.12 for xz-plane phasing and Figure B.13 for yz-phasing) the maximum radiation occurs off of true endfire $\theta = 90°$, at approximately $\theta = 60°$ with a maximum gain of 14.6 dBi and 13.2 dBi, respectively. The off-endfire maximum gain is attributed to the same mechanisms seen in the 2×2 array and shares similar effects on the endfire radiation pattern. Gain versus frequency for all configurations and are plotted in Figure B.14. Using these plots in conjunction with the radiation plots, a qualitative comparison can be made between the two different endfire phasing scenarios, further

demonstrating the effects of asymmetry in the array. The measured radiation behavior is in good agreement with the results predicted in Section B.1 aside from the decrease in the non-dominant polarization, which is an effect of the interaction of the elements physical radiating mechanisms and increasing ground plane dimensions.

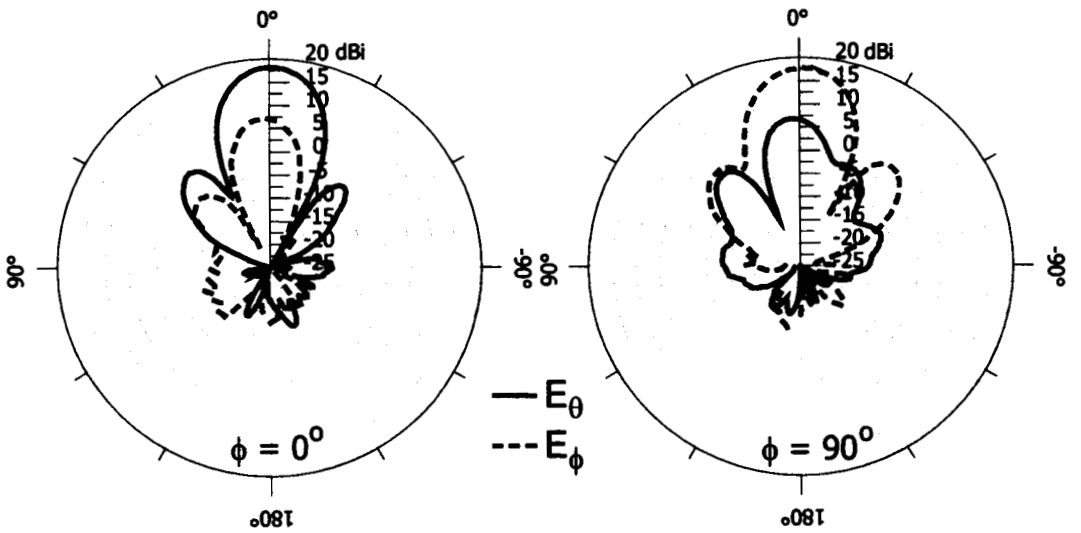

Figure B.11. Measured elevation radiation patterns for the 4 × 4 array in broadside configuration.

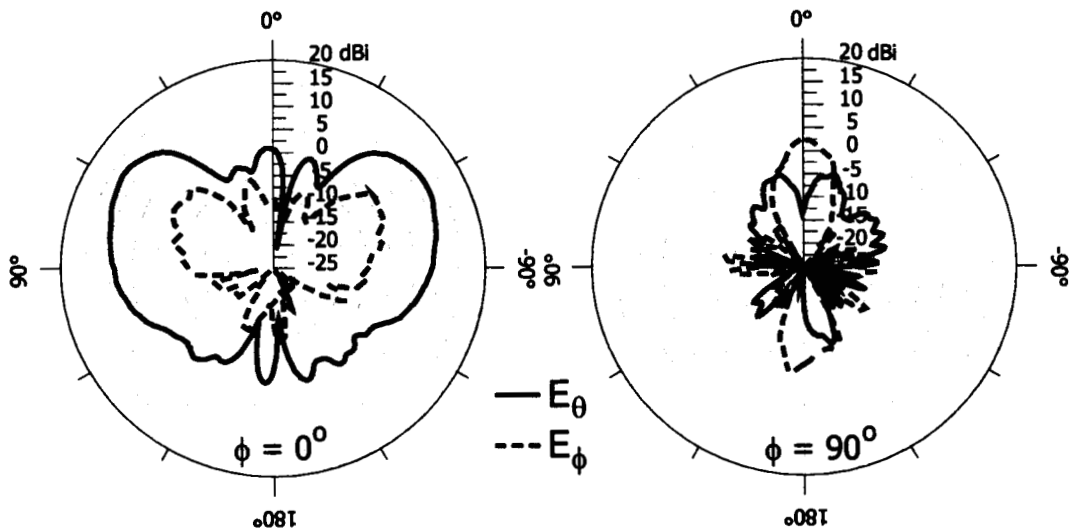

Figure B.12: Measured elevation radiation pattern for the 4 × 4 array in the endfire configuration, phase-reversal in xz-plane ($\varphi = 0°$), in-phase in yz-plane($\varphi = 90°$).

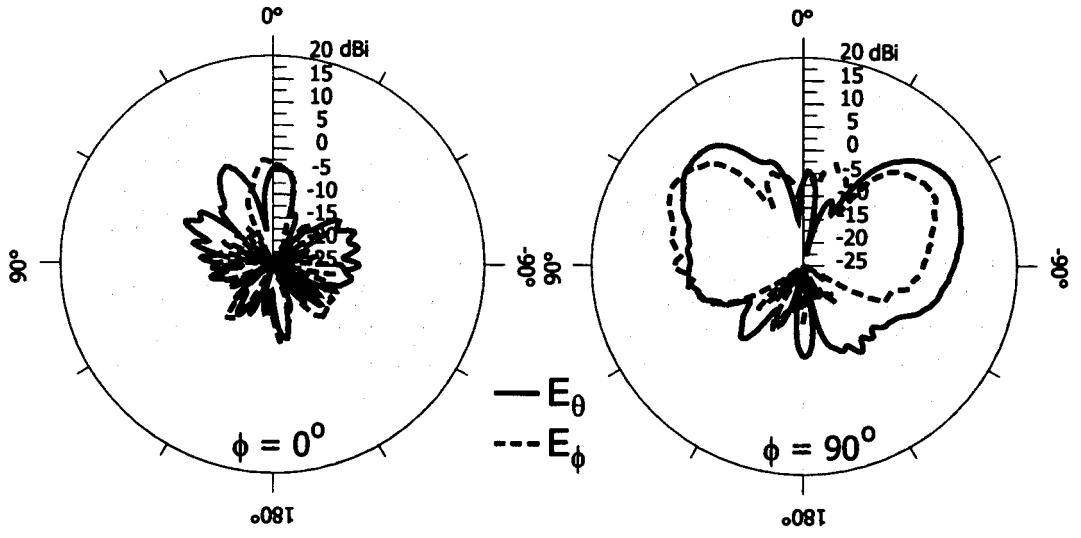

Figure B.13: Measured elevation radiation pattern for the 4 × 4 array in the endfire configuration, phase-reversal in yz-plane (φ = 0°), in-phase in xz-plane(φ = 90°).

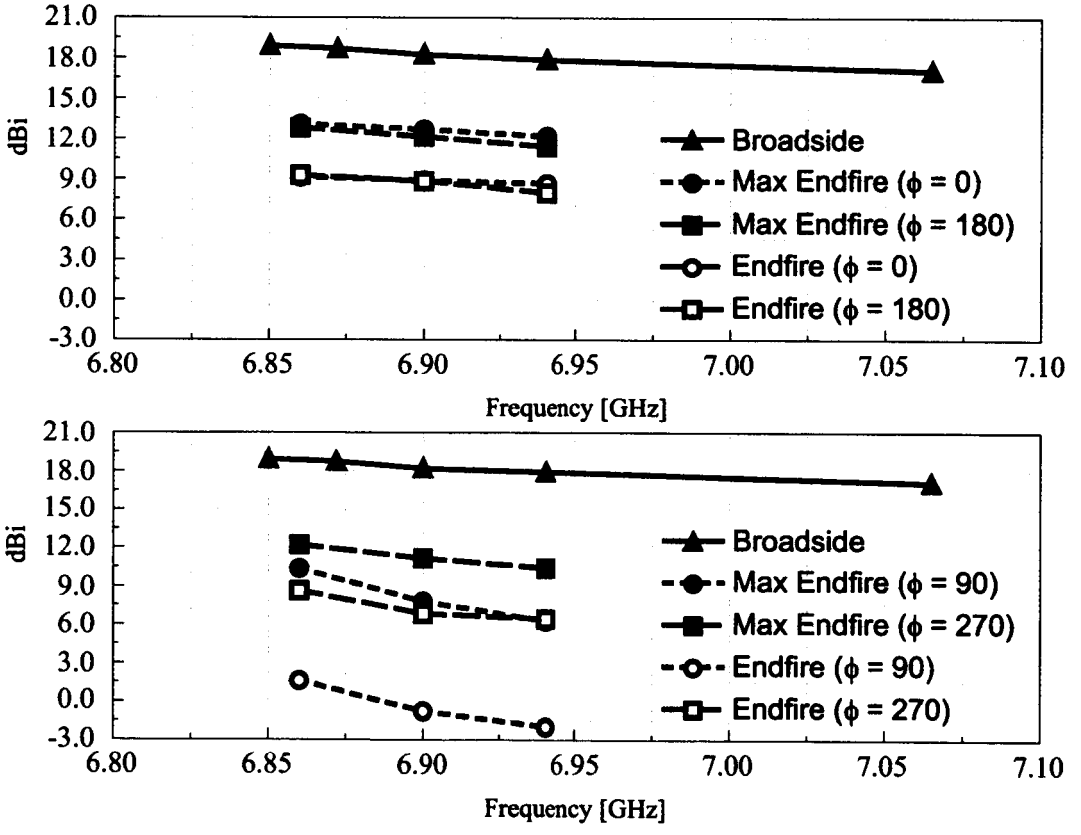

Figure B.14: Measured gain vs. frequency for broadside and endfire configurations with phase reversal in xz-plane (top) and yz-plane (bottom).

B.3.3.3 Mutual Coupling

Measured results of inter-element coupling are shown in Figure B.15 (endfire) and Figure B.16 (broadside). Each series of plots examines the mutual coupling from an active element in all 4 perimeter corners as well as an inner diagonal set of elements (11, 41, 14, 44, 23, and 32 in Figure B.5). This coupling behavior, in conjunction with the individual element VSWR bandwidths and array radiation characteristics, punctuate the effects of symmetry and element position as the dimension of the array increase. The broadside configuration, with a broadened overall VSWR bandwidth and little radiation pattern asymmetry, indicate the overall effects of geometric asymmetry for that configuration limit the effects of coupling on the performance of the array. This is demonstrated in the magnitude of the inter-element coupling, which quickly tapers off in the row direction and is only slightly increased in the column direction; showing dissimilar variations amongst all the element positions. Conversely, inter-element coupling in the endfire configuration conveys a higher presence of geometric symmetry with an increased magnitude of coupling to neighboring elements. This results in the degenerative pattern effects previously discussed (Figure B.11), observed when phasing in the yz-plane (where the asymmetric variation along the rows is greatest), and is also the direction (along y) that has the closest inter-element spacing.

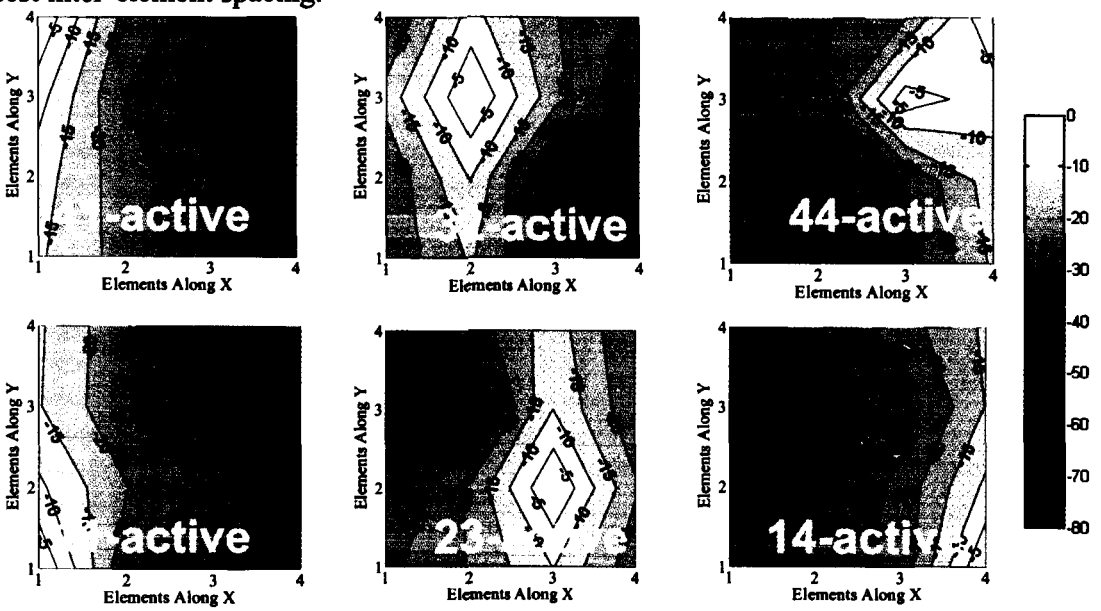

Figure B.15: Measured mutual coupling (dB) in the 4 × 4 array in endfire configuration.

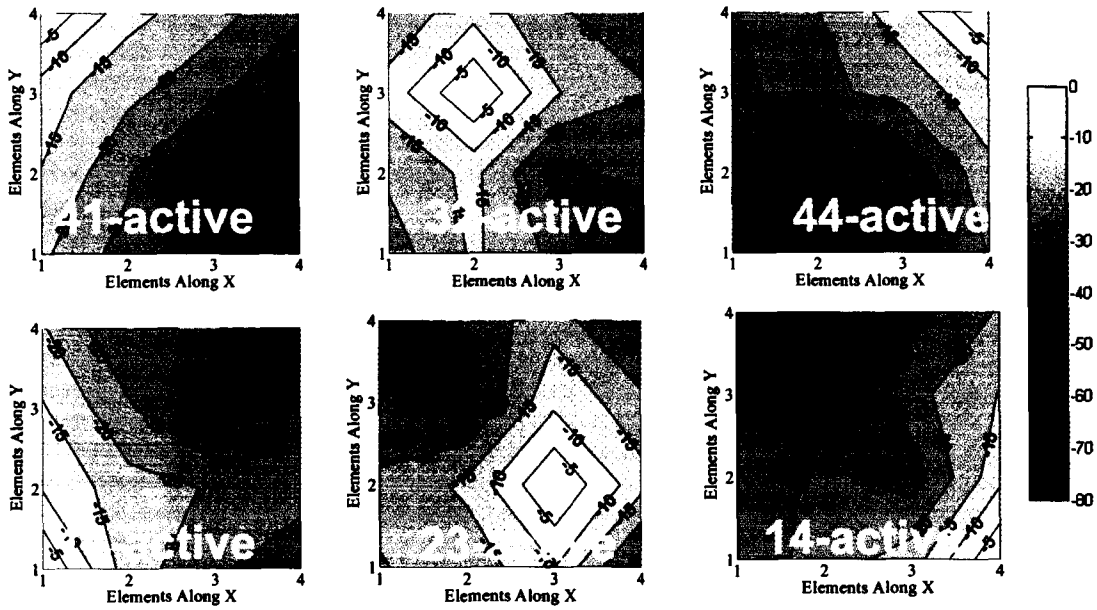

Figure B.16: Measured mutual coupling (dB) in the 4 × 4 array in broadside configuration.

B.4 Summary of Endfire-Broadside Behavior of Reconfigurable Arrays

In this section, the behavior and performance potential of small arrays comprised of radiation reconfigurable antennas has been demonstrated. This provides the groundwork for further studies of beam steering and similar types of arrays by using a fundamental process of superposition for determining the necessary conditions by which the array can recover the reconfigurable radiation characteristics. In both fabricated antenna arrays, the effects from placement/position of the individual antenna elements in the array is very evident, and was observed in several form with parallels occurring between the symmetry of the antenna element and its behavior in the array. These results indicate that the element configuration with the most asymmetric geometry has the least undesirable behavior when operated in the dense array setting. This manifested itself in the expansions/contractions of the individual element's 2:1 VSWR bandwidth and the shifting of the center frequency, but was most evident in the degenerative pattern effects observed in the larger array (4×4). This trend warrants further investigation into these effects, since the effects are commonly observed [e.g., 2, 3] in the array behavior of traditional elements.

B.5 References for Section B

[1] A. O. Boryssenko and D. H. Schaubert, Some lessons learned about truncation effects in wideband Vivaldi array, 327 - 354, *Proc. 2003 Antenna Applications Symposium*, Allerton Park, Monticello, IL, 2003, pp. 307 – 319.

[2] J. Yen, Coupled surface waves and broadside arrays of end-fire antennas, *IRE Transactions on Antennas and Propagation*, vol. 9, no. 3, 1961, pp. 296 -304.

[3] W. Wasylkiwskyj and W. Kahn, An explicit relation between mutual coupling and the pattern of an antenna array, *1966 IRE International Convention Record*, March 1966, pp.167 -171.

C. Performance of antenna in array configurations for beam scanning operation

C.1 Beam Scanning in Small Arrays

To begin to evaluate the performance of pattern reconfigurable antennas in phased arrays for beam steering, we studied small 1×4 arrays of reconfigurable elements and compared them to standard rectangular microstrip arrays with the same number of elements. Extensive simulation and measurement studies were undertaken. Here we present a sample of the results. Figure C.1 shows three arrays for comparison. The patch antennas are configured for minimal inter-element coupling, while the reconfigurable elements are oriented for maximum inter-element coupling. Comparisons in this situation represent the worst possible case for the reconfigurable elements.

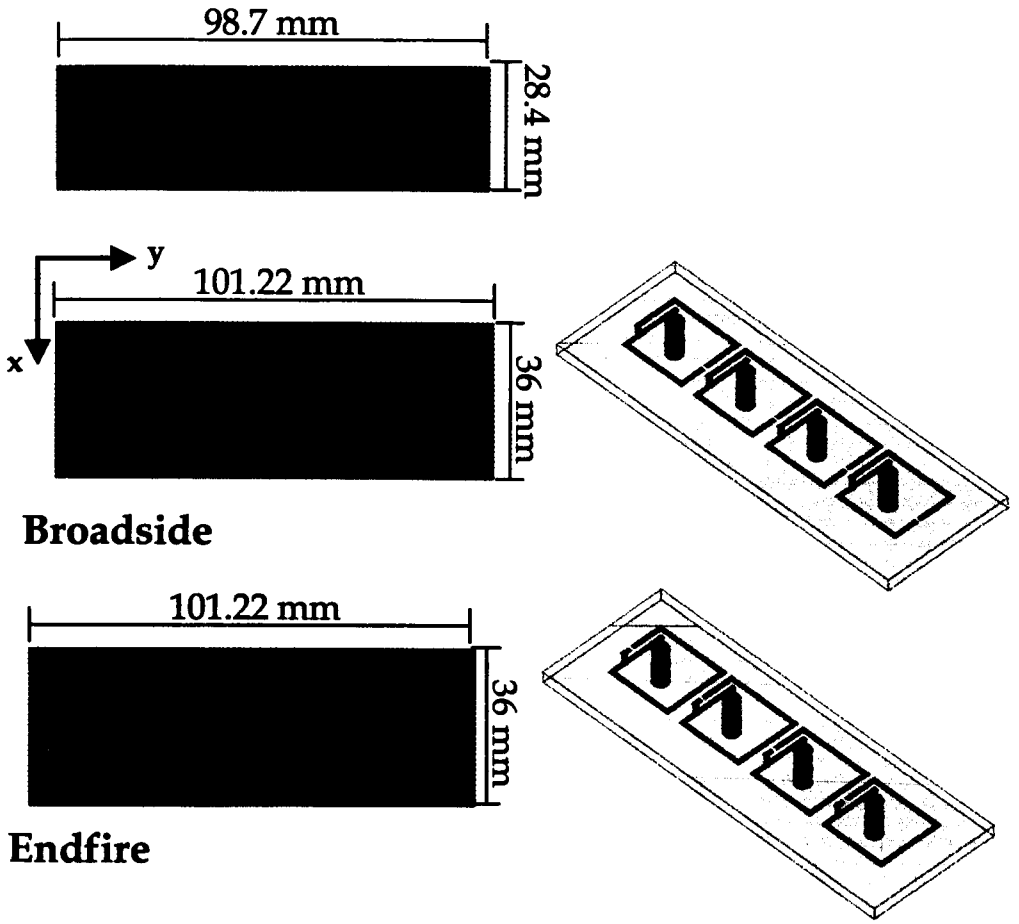

Figure C.1: Sample configurations of 1×4 arrays to evaluate beam scanning capabilities of pattern reconfigurable antennas.

C.2 Results

For each configuration, input impedance, VSWR, and radiation patterns were simulated and measured for a range of scan angles from broadside to horizon. Simulations are shown here for

brevity. Figure C.2 shows the simulated VSWR for each of the configurations shown in Figure C.1 for each element.

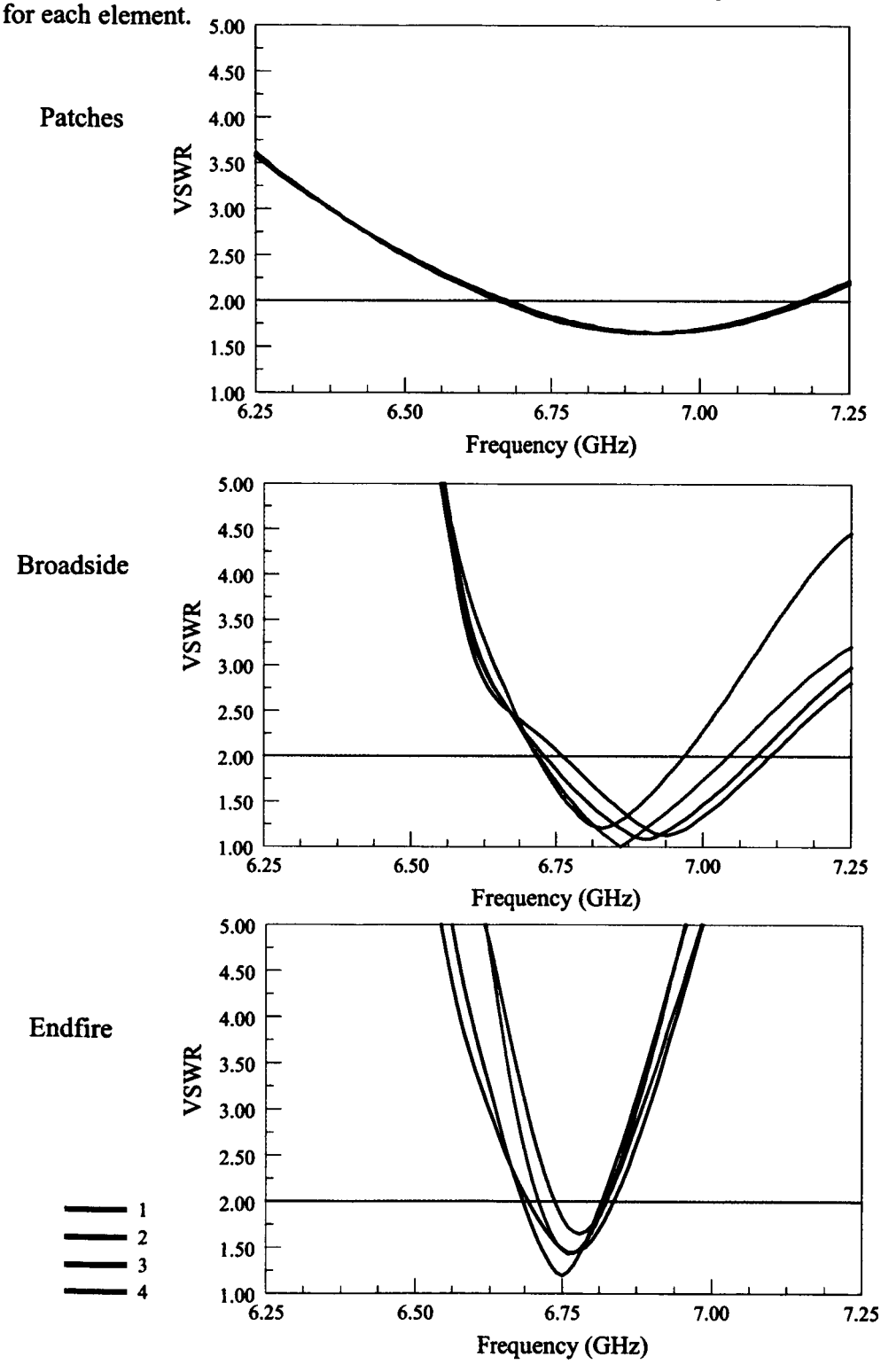

Figure C.2: Simulated VSWR for each element in each 1×4 array.

The reconfigurable arrays have approximately 60 MHz of shared bandwidth around 6.75 GHz. Our results indicate that one can switch between the modes of the reconfigurable antenna to obtain larger scan angles with larger isolation from sidelobes that appear at large scan angles. There is a tradeoff of absolute gain (of about 1.5 dB) in the endfire mode of the reconfigurable array, but this is compensated for by a larger difference between the main beam level and the magnitude of the highest sidelobe. Figure C.3 illustrates the patterns obtained for a scan angle of –40 degrees.

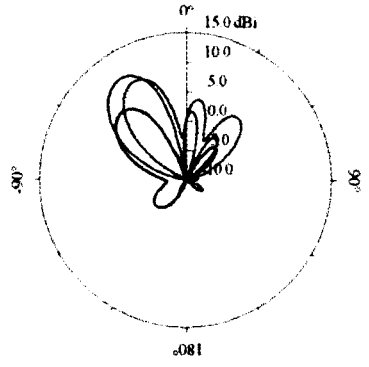

Figure C.3: Simulated patterns at –40° scan angle (green: patch; orange: broadside; blue: endfire).

Table C.1: Calculated values of the difference between the pattern maximum and the next highest sidelobe level for various scan angles with the three arrays.

Scan Angle	Patch	Broadside	Endfire
0°	13.01	12.45	0.51
-20°	11.54	8.74	4.38
-30°	10.08	6.16	5.87
-40°	8.32	2.79	8.06
-50°	6.20	-2.83	11.05
-60°	3.71	-8.68	8.58

Table C.1 provides the calculated differences between the main beam maximum and the next highest sidelobe level. Up to a scan angle of –40°, the patch and broadside configurations perform well, with the patch having a greater distinction between the main beam and the sidelobe

level. However, as the scan angle increases past -40^0, the difference between the main beam and the sidelobe level decreases for the patches, but maintains a high level when the reconfigurable elements are in the endfire mode. This study helps to illustrate the possible benefits having pattern reconfigurability at individual elements in a phased array. More detailed studies of a variety of arrays and configurations can be found in [1].

C.3 References for Section C

[1] M.S. Thesis: *Beam Steering in Phased Arrays Using a Pattern Reconfigurable Antenna*, Kevin N. Hietpas, University of Illinois at Urbana-Champaign, December 2004.

D. Simulation of antennas in infinite phased arrays

As part of this work, the antennas were simulated as elements in infinite phased arrays using a time domain integral equation (TDIE)-based solver for doubly periodic structures. Several arrays were simulated at 2.44 GHz and 6.9 GHz. For each of these arrays in the two main antenna configurations (endfire and broadside) the input impedance and VSWR are provided. These results also agree well with simulations of infinite arrays performed in HFSS not provided here.

Figures D.1-D.4 provide the input impedance and VSWR plots for the 2.44 GHz design, and Figures D.5-D.8 provide the same data for the 6.9 GHz design. Each antenna is evaluated in both broadside and endfire modes. In the simulations, vias are modeled using narrow strips and the in-line open circuit is modeled using a 1mm wide gap. The endfire mode is realized via phasing the elements along y-direction with a progressive 180-degree phase shift.

The simulations indicate, as one would expect, that the coupling between elements in an infinite or very large array has a noticeable effect on the input impedance of the individual elements and also results in a frequency shift in the case of the endfire mode of the antenna. Our work with smaller arrays of these elements indicate that these effects can largely be compensated by small changes in element design, in particular, the locations of the switches and small changes to element spacing and the distance between the coupled arms in the individual elements.

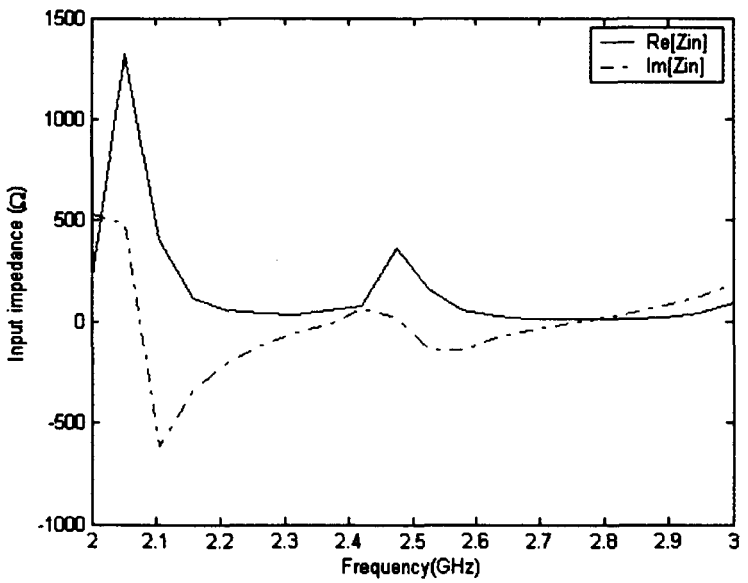

Figure D.1: Impedance plot of the broadside infinite reconfigurable antenna array (2.44 GHz design).

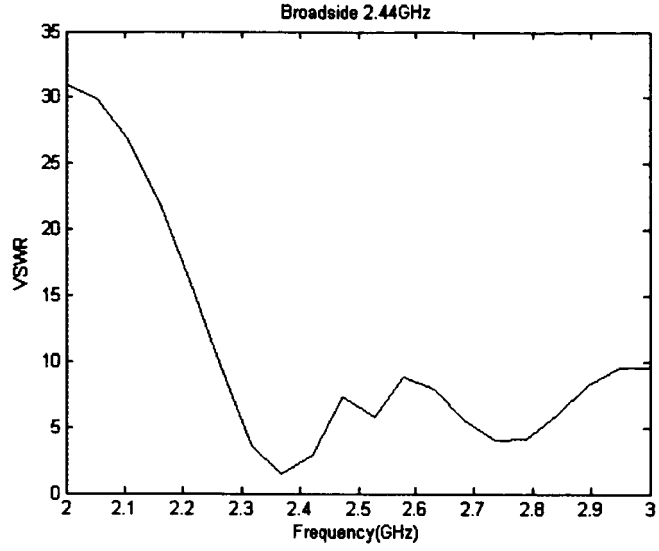

Figure D.2: VSWR plot of the broadside reconfigurable antenna array (2.44GHz design

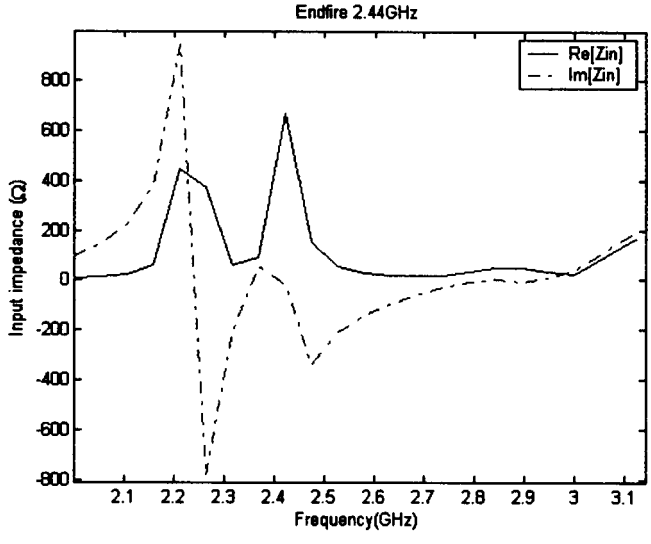

Figure D.3: Impedance plot of the endfire infinite reconfigurable antenna array phased along y-direction (2.44 GHz design).

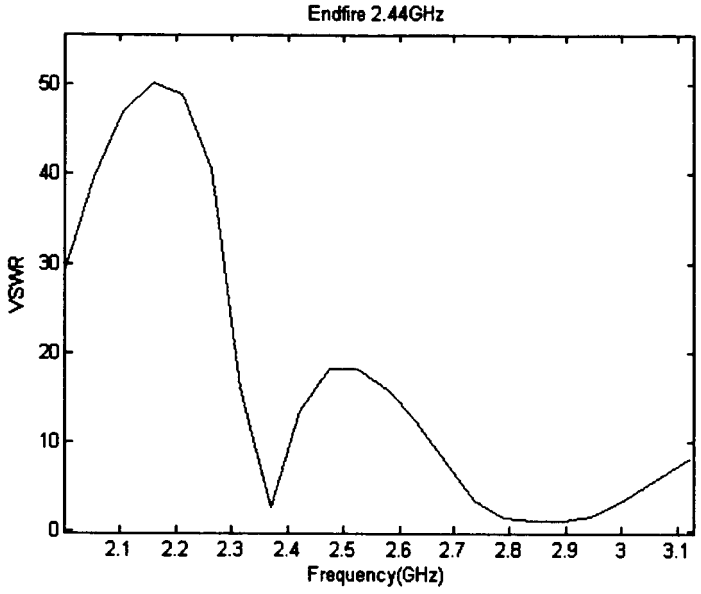

Figure D.4: VSWR plot of the endfire infinite reconfigurable antenna array phased along y-direction (2.44 GHz operation).

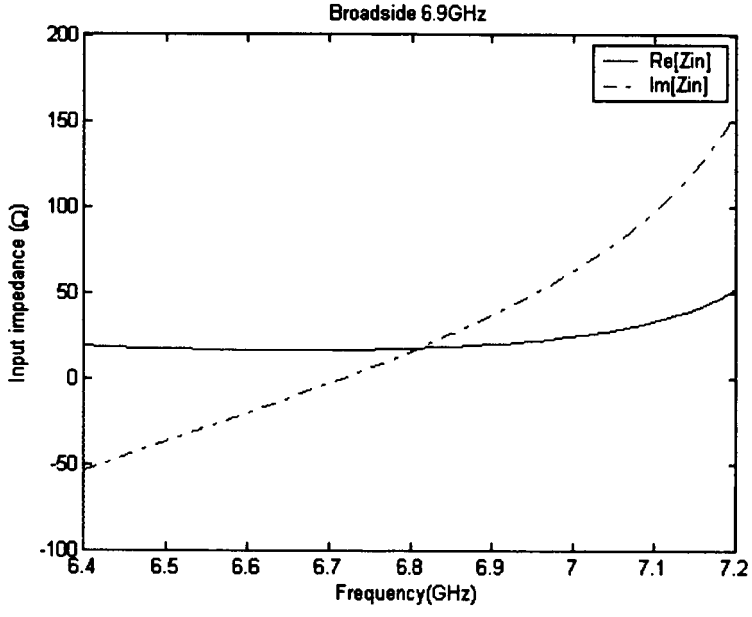

Figure D.5: Impedance plot of the broadside infinite reconfigurable antenna array (6.9 GHz operation).

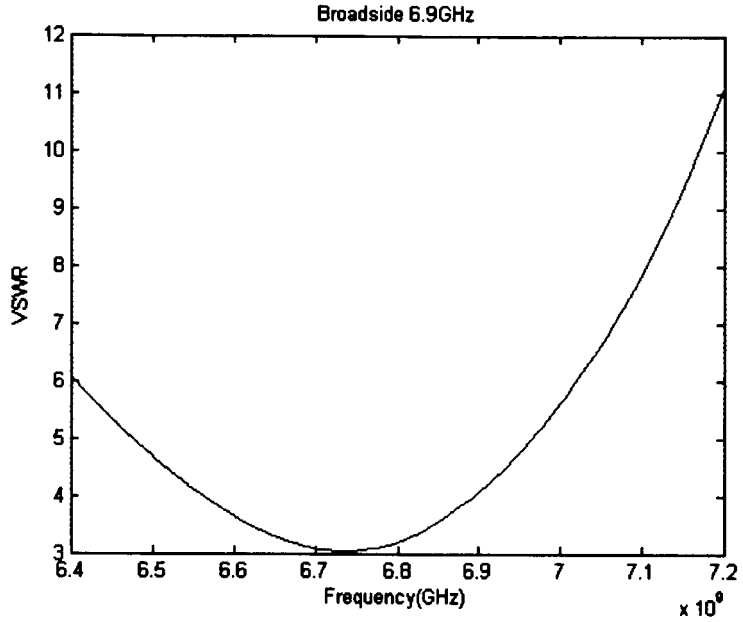

Figure D.6: VSWR plot of the broadside infinite reconfigurable antenna array (6.9 GHz operation).

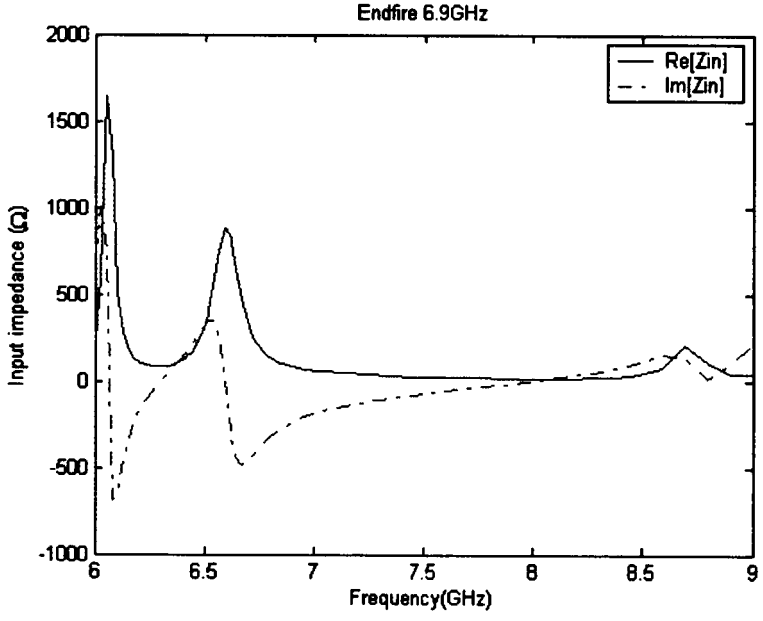

Figure D.7: Impedance plot of the endfire infinite reconfigurable antenna array phased along y-direction (6.9 GHz operation).

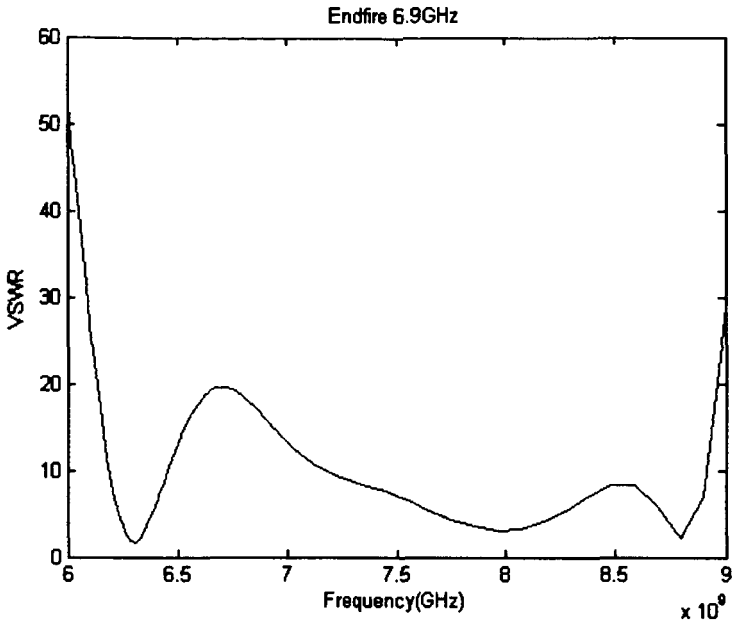

Figure D.8: VSWR plot of the endfire infinite reconfigurable antenna array phased along y-direction (6.9 GHz operation).

E. Demonstration of antenna with commercially-available RF MEMS switches

One of the most challenging aspects of this project was the integration of packaged, commercially-available RF MEMS switches into the antennas. We spent a great deal of time trying to implement CPW RF MEMS switches from Teravicta into our antennas. The results of this work were disappointing on a number of levels. First, the engineering samples that we purchased had variable quality. Second, the switches were susceptible to sporadic stiction problems. In the end, the design and packaging of the switches made them inappropriate for integration into the 6.9 GHz prototypes. This was mainly due to mode-conversion problems between the microstrip mode of the antenna and the CPW mode necessary for proper switch operation. As a result, even when the switches were operating properly, the antenna currents were not distributed properly because of disturbances caused by the discontinuities presented by the switches.

To alleviate these problems, we turned to another company, Radant MEMS, to obtain in-line microstrip-based RF MEMS switches on silicon configured for single-pole, single throw operation with an actuation voltage of approximately 60 V (part number SPST-RMSW100). These switches were much less expensive than those from Teravicta, had simpler bias network requirements and layouts, and were more appropriate for integration into a microstrip-based design. The block diagram and a photograph of one of the Radant switches are shown in Figure E.1.

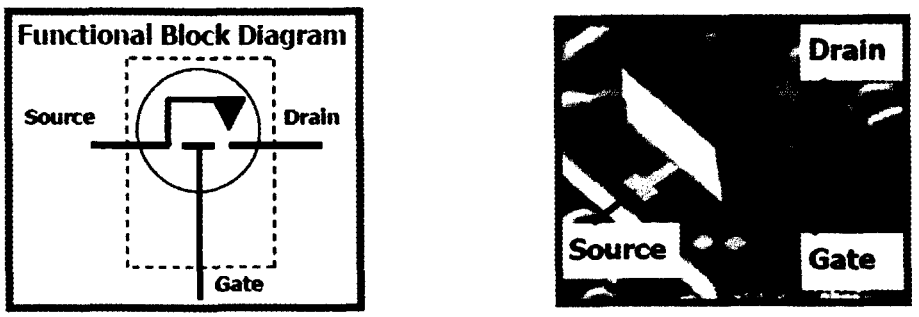

Figure E.1: Block diagram (left) and photograph (right) of Radant RF MEMS switch. (Courtesy of Radant MEMS.)

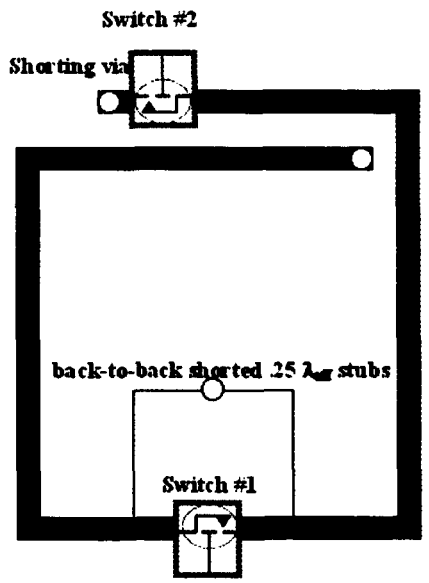

Figure E.2: Diagram showing DC bias configuration for switches.

We made one small change to the package of the switches – we sanded off the ground plane on the bottom side of each RF MEMS switch with an emory cloth. This allowed the switches to operate in a microstrip mode compatible with antenna operation. High strength adhesive (super glue) was used to seat switch onto antenna substrate. By sanding off the ground plane of the switch, the gate was no longer isolated from the RF connection. The switch actuation occurs as a result of a potential difference between the source and gate. The drain voltage can be varied to reset the switch if needed, but is kept at 0 VDC for this work. Once the ground plane of the switch was removed, the switch appeared as a very thin microstrip line when it was closed, resulting in an additional small inductance, which was tuned out with a short microstrip stub. The DC potential of all spiral sections are tied to common ground (0 VDC) using the shorting via and back-to-back .25 λ_{eff} shorted stubs placed inside the spiral around switch #1 as shown in

Figure E.2. To actuate the switches, the applied bias voltages V_{Bias} are routed from the gate through connections to the backplane of the substrate.

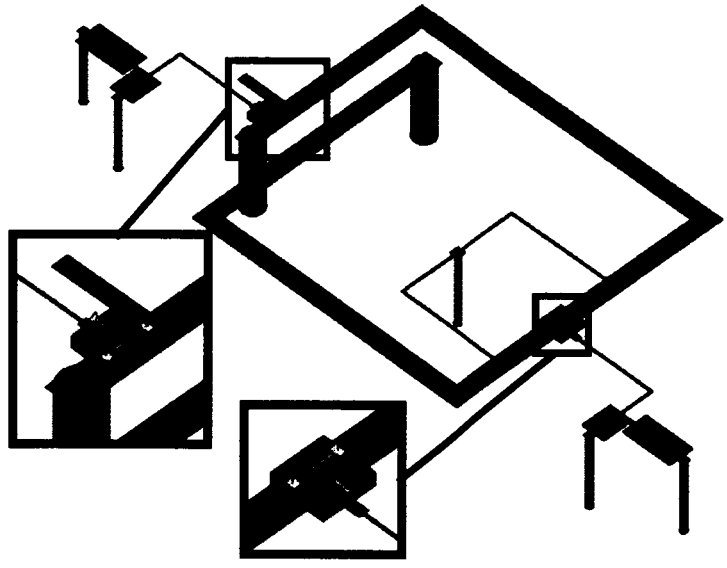

Figure E.3: Simulated reconfigurable antenna including all bias lines and circuitry.

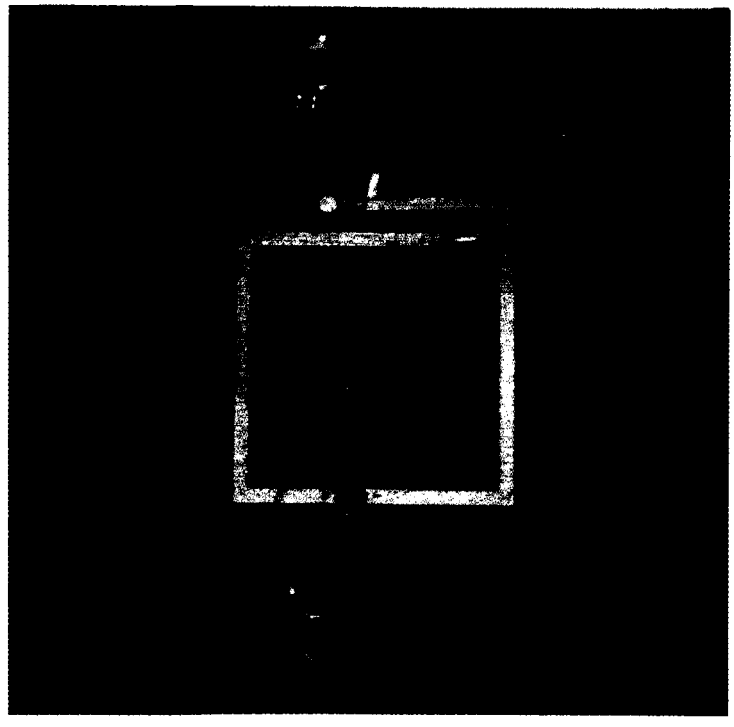

Figure E.4: Photograph of pattern reconfigurable microstrip antenna with packaged RF MEMS switches from Radant MEMS with operation at 6.35 GHz.

The antenna shown in Figure E.3 was simulated using HFSS and the location and length of the tuning stub for Switch #2 was verified. A photograph of the fabricated antenna is shown in Figure E.4. Measured VSWR for the antenna's two modes is presented in Figure E.5.

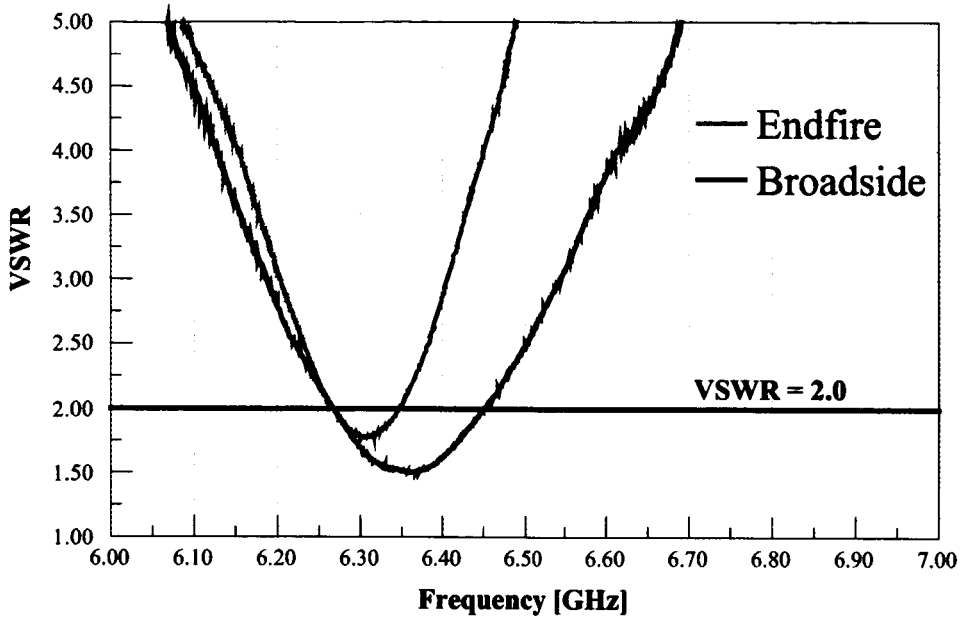

Figure E.5: Measured VSWR of two modes (endfire and broadside) of pattern reconfigurable antenna with Radant MEMS switches.

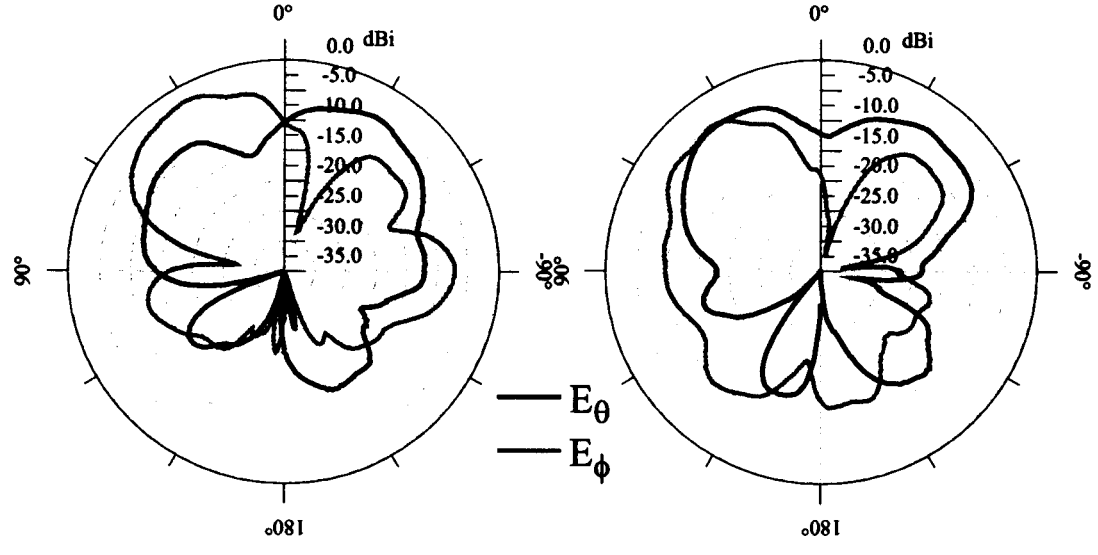

Figure E.6: Measured endfire patterns ($\phi = 0^0$, left; $\phi = 90^0$, right) of pattern reconfigurable antenna with Radant MEMS switches.

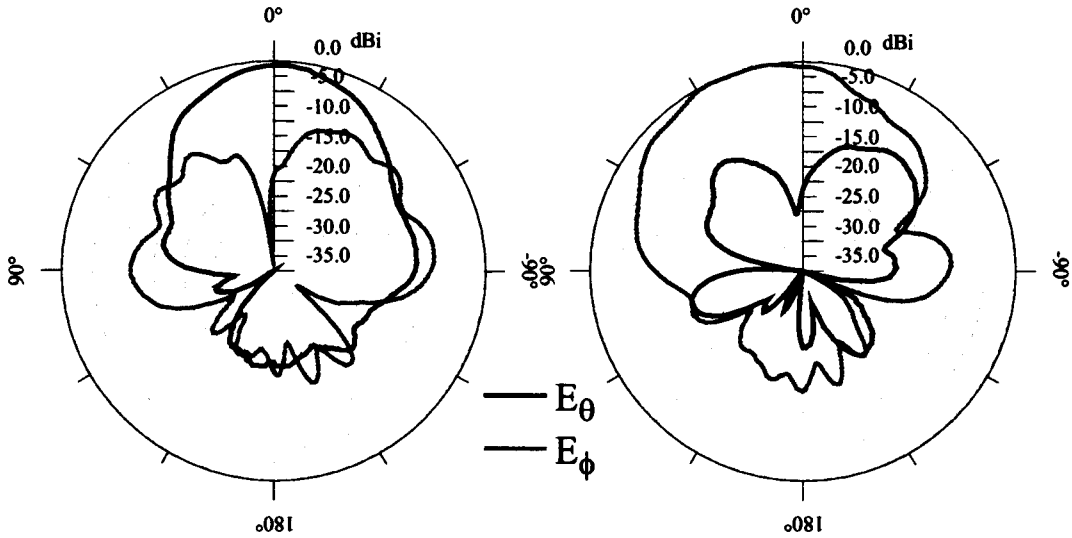

Figure E.7: Measured broadside patterns ($\phi = 0^0$, left; $\phi = 90^0$, right) of pattern reconfigurable antenna with Radant MEMS switches.

Measured radiation patterns for this antenna are shown in Figures E.6 and E.7 for endfire and broadside configurations, respectively. It is clear that this design works as intended and has operation very close to that already demonstrated with soldered through connections in place of the switches. **This data is the first known measurement of a pattern reconfigurable microstrip antenna equipped with commercially-available RF MEMS switches.**

F. Design of antenna/RF MEMS switch combinations for direct simultaneous fabrication

We have finalized the designs for both frequency- and pattern-reconfigurable antennas at 26.5 GHz. We have developed several different designs that are compatible with a variety of IC fabrication processes. We are working with Prof. Milton Feng's group at UIUC as well as Prof. John Papapolymerou's group at Georgia Tech to fabricate the antennas with integrated RF MEMS switches for operation at 26.5 GHz.

F.1 Designs for CPW RF MEMS Switches

The UIUC switch is a CPW design, so we have two antenna designs that are compatible with this switch. Results from these designs are shown in Figures F.1 - F.3. The design in Figure F.1 is a modified folded dipole design that exhibits frequency reconfigurability.

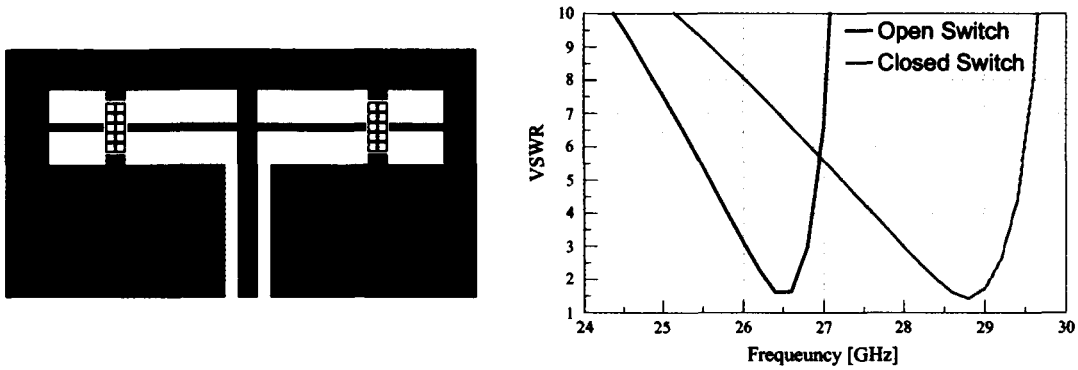

Figure F.1: [Left] Modified folded dipole design compatible with CPW RF MEMS switches. [Right] Simulated frequency reconfigurability when two switches are closed, making the effective length of the slot shorter.

F.2 Designs for In-Line Microstrip RF MEMS Switches

The second design utilizes a geometry more closely approximating our previous low-frequency prototypes. This design will implement in-line microstrip-based switches fabricated at Georgia Tech. The layout and details of the design are shown in Figure F.2. Figure F.3 shows the simulated performance of the integrated reconfigurable antenna.

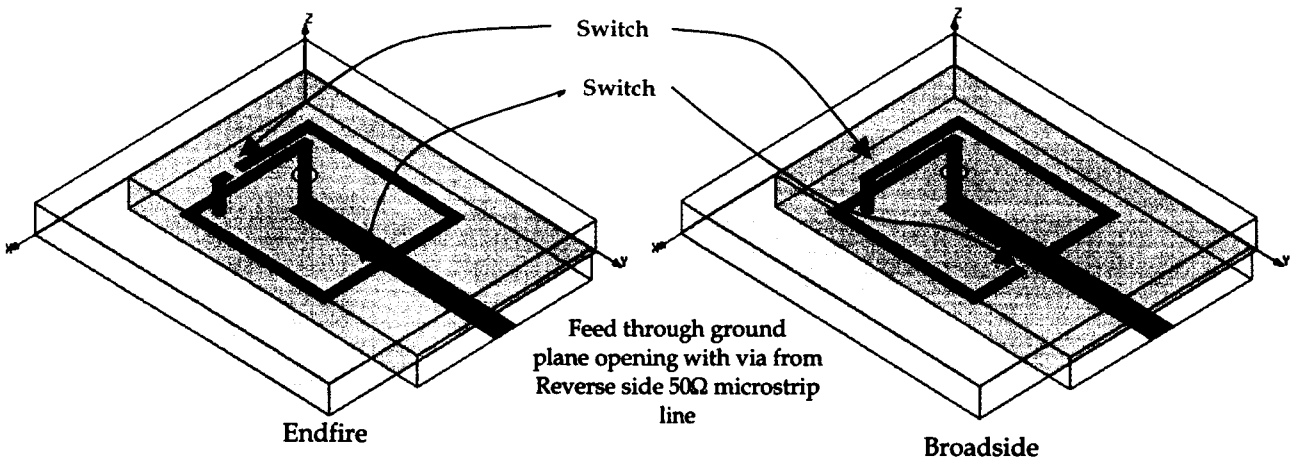

Figure F.2: This antenna design is suitable for the in-line microstrip RF MEMS switch available from Georgia Tech. The design is fabricated on 410 μm high resistivity silicon substrate with relative permittivity of 11.7 and a conductivity of 10^{-6} S/m for operation at 26 GHz.

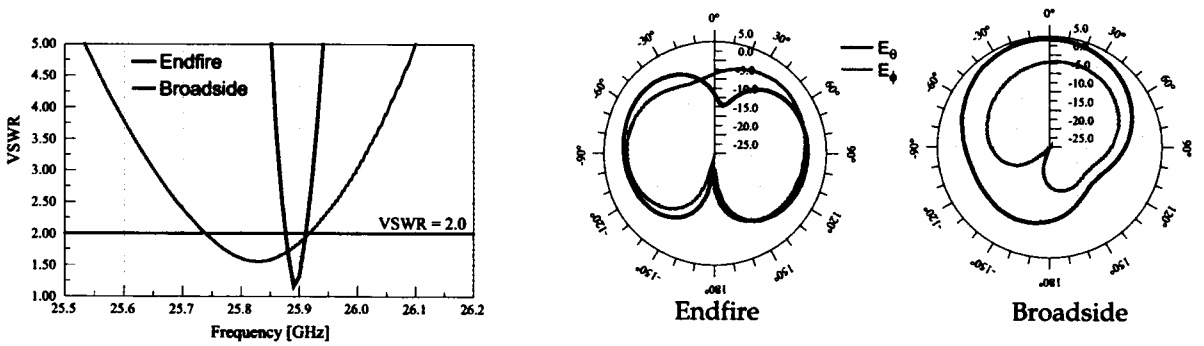

Figure F.3: Simulated results (VSWR and patterns in the $\phi=0^{\circ}$ plane) from design shown in Figure F.2. Both shared bandwidth and pattern reconfigurability are preserved from the original low-frequency prototype designs.

F.3 Future Work

We plan to continue to work on these antennas by soliciting funding from a variety of government and commercial interests. In particular, we are going to concentrate our efforts on the direct design and fabrication of specialized RF MEMS switches with the antennas begun here. In this way, we will be avoiding many of the packaging and material issues that we encountered in our efforts to integrate commercially-available switches with the antennas.

Conference Papers and Journal Articles supported by this grant to date

1. J. T. Bernhard, "Compact single-arm square spiral microstrip antenna with tuning arms," *Proc. IEEE Antennas and Propagation Soc. International Symp.*, vol. 2, 2001, pp. 696-699.

2. (*Invited Paper*) G. Huff, S. Zhang, J. Feng, and J. T. Bernhard, "Performance and packaging issues of novel reconfigurable antennas in laptop computers," *Proc. 2002 IEEE/URSI International Symposium on Antennas and Propagation*, vol. URSI, p. 178.

3. S. Zhang, G. Huff, J. Feng, and J. T. Bernhard, "Design model development for spiral microstrip antennas," *Proc. 2002 IEEE/URSI International Symposium on Antennas and Propagation*, vol. URSI, p. 286.

4. G. H. Huff, G. Cung, and J. T. Bernhard, "Investigation of polarization purity and port isolation in circularly polarized microstrip patch antennas with ground plane edge serrations." *Proc. 2002 Antenna Applications Symposium*, Allerton Park, Monticello, Illinois, 2002, pp. 307-319.

5. G. Huff, J. Feng, S. Zhang, and J. T. Bernhard, "A novel radiation pattern and frequency reconfigurable single turn square microstrip spiral antenna." *IEEE Microwave and Wireless Components Letters,* vol. 13, no. 2, pp. 57-59, February 2003.

6. G. H. Huff, J. Feng, S. Zhang, G. Cung, and J. T. Bernhard, "Directional reconfigurable antennas on laptop computers: simulation, measurement, and evaluation of candidate integration positions." In review at *IEEE Transactions on Antennas and Propagation.*

7. [Keynote Address] J. T. Bernhard, "Reconfigurable Antennas and Apertures: State-of-the-Art and Future Outlook," *Proc. SPIE Conf. on Smart Electronics, MEMS, BioMEMS, and Nanotechnology*, vol. 5055, March 2003.

8. G. H. Huff, J. Feng, S. Zhang, J. T. Bernhard, "Behavior of Pattern and/or Frequency Reconfigurable Antennas in Small Arrays," *Proc. 2003 IEEE/URSI Int. Symp. on Antennas and Propagation*, June 2003.

9. G. H. Huff, J. Feng, and J. T. Bernhard, "A Small Array of Boresight to Endfire Radiation Reconfigurable Antennas." *Proc. Antenna Applications Symposium*, Allerton Park, Monticello, Illinois, 2003.

10. J. T. Bernhard, "Antennas for Multifunction RF Systems: Current Work and Future Directions," Poster presented at the DARPA/ONR Workshop on Future Directions for Multifunction RF Systems, November 19-21, 2003.

11. M.S. Thesis: *A Pattern and Frequency Reconfigurable Microstrip Spiral Antenna*, Gregory H. Huff, December 2003. Continuing at UIUC for Ph.D.

12. J. T. Bernhard, G. H. Huff, J. Feng, and S. Zhang, "Radiation pattern reconfigurable antennas and arrays: operation and switch integration," in *Proc. URSI National Radio Science Meeting*, Jan. 2004, p. 114.

13. J. T. Bernhard, G. H. Huff, J. Feng, and S. Zhang, "Individually reconfigurable elements in arrays: operation from broadside to endfire," *Proc. GOMACTech-2004*, Monterey, CA, March 2004.

14. G. H. Huff, T. L. Roach, and J. T. Bernhard, "A study of diversity performance of integrated combinations of fixed and reconfigurable antennas on portable devices," *Proc. 2004 IEEE/URSI Int. Symp. on Antennas and Propagation*, Monterey, CA, v. URSI, June 2004, p. 137.

15. G. H. Huff, T. L. Roach, and J. T. Bernhard, "Conformal integration of broadside to endfire radiation reconfigurable antennas onto canonical structures," *Proc. 2004 IEEE/URSI Int. Symp. on Antennas and Propagation*, Monterey, CA, v. URSI, June 2004, p. 138.

16. K. Hietpas, G. H. Huff, and J. T. Bernhard, "Investigation of phased array beamsteering using reconfigurable antennas," *Proc. IASTED Int. Conf. on Antennas, Radar, and Wave Propagation*, July 2004, pp. 41-44.

17. G. H. Huff and J. T. Bernhard, "Effects of mutual coupling in arrays of radiation reconfigurable antennas," *Proc. IASTED Int. Conf. on Antennas, Radar, and Wave Propagation*, July 2004, pp. 92-96.

18. (*Invited Paper*) G. H. Huff, K. Hietpas, and J. T. Bernhard "Reconfigurable microstrip antennas in phased arrays: performance and potential," *Proc. 2004 Progress in Electromagnetics Research Symposium (PIERS) Symposium*, Nanjing, China, August 2004, p. 17.

19. G. H. Huff and J. T. Bernhard, "Analysis of a radiation and frequency reconfigurable microstrip antenna," Finalist in student paper competition, *Proc. 2004 Antenna Applications Symposium*, Sept. 2004, pp. 175-191.

20. G. H. Huff, J. Feng, S. Zhang, and J. T. Bernhard, "Directional reconfigurable antennas on laptop computers: simulation, measurement, and evaluation of candidate integration positions." *IEEE Transactions on Antennas and Propagation*, vol. 52, pp. 3220-3227, December 2004.

21. M.S. Thesis: *Beam Steering in Phased Arrays Using a Pattern Reconfigurable Antenna*, Kevin N. Hietpas, December 2004.

22. G. H. Huff and J. T. Bernhard, "A radiation and frequency reconfigurable microstrip antenna: single element behavior and cavity model." In review at *IEEE Transactions on Antennas and Propagation.*

23. G. H. Huff, J. Feng, and J. T. Bernhard, "Broadside and endfire phased array behavior of switched broadside-to-endfire radiation reconfigurable microstrip antennas." In review at *IEEE Transactions on Antennas and Propagation.*